Circuits and Systems
Mekelweg 4,
2628 CD Delft
The Netherlands
https://cas.tudelft.nl/

MSc Thesis

Sensor-to-Cell Height Estimation for Conductivity Estimation in Cardiac Cells

Cees H. Kos

Faculty of Electrical Engineering, Mathematics and Computer Science
Delft University of Technology

Sensor-to-Cell Height Estimation for Conductivity Estimation in Cardiac Cells

Thesis

submitted in partial fulfilment of the
requirements for the degree of

Master of Science

in

Electrical Engineering

by

Cees H. Kos
born in Amsterdam, The Netherlands

This work was performed in:

Circuits and Systems Group
Department of Microelectronics
Faculty of Electrical Engineering, Mathematics and Computer Science
Delft University of Technology

Delft University of Technology

Abstract

The heart is one of our vital organs. It functions by periodically contracting in a characteristic rhythmic way. It can occur, that this rhythmic behaviour is distorted, disrupted or otherwise affected by abnormalities in the tissue. These conditions are consequently referred to as cardiac arrhythmias. One kind is of specific interest, called atrial fibrillation (AF). Cardiac arrhythmias are often harmless, but can potentially be fatal. To further study AF, methods have been developed to estimate the conductivity of cardiac cells based on the measured electrical signals. These problems are said to be ill-posed. In addition, other parameters besides the conductivity are involved which have to be estimated jointly or assumed to be known otherwise. The goal of this project was to consider in particular one of the parameters in the electrogram (EGM) model: the sensor-to-cell height. The foremost effect of this height is the spatial low-pass filtering effect it applies on data received by the sensors.

First, we studied the effect of the height as a parameter in the model when used for conductivity estimation. To that end, a detector was built with which we can explain the effect of all involved parameters on the ability to accurately estimate any parameters of interest. From the results, it can be concluded that as the height decreases, decisions made using the detector become more accurate.

In addition, we considered the case where the height is unknown and is estimated, thus possibly including estimation errors. The focus was on the consequences of making errors in the estimation of the height with respect to conduction block detection and conductivity estimation. Specifically, an underestimate of the height will increase the threshold in the conduction block detector, making it easier to detect conduction blocks, and low conductivity values are drawn to the sensor. For overestimation of the height, the opposite holds true, as well as high conductivity values are drawn to the sensor, resulting in the suppression of blocks in the vicinity of sensor locations.

Lastly, the effort was made to estimate the height. Here, the optimisation problem of height estimation was formalised and derived as its implementable form. Important to note is that in this case, a simplified EGM model was assumed in order to mimic and estimate cell-specific effects, i.e. the cell conductivities. Then, the height was estimated in various situations to study its behaviour and performance under different conditions. It was seen that as the average height increases, it becomes harder to obtain good estimates of the height map and the diffusive current weights. If we instead increase the maximum amplitude of the height, the error gets larger as well. We also tested for different spatial frequencies of the height map, with higher spatial frequencies resulting in larger errors. The error also seems to depend on how much variations in the height coincide with conductivity blocks. Lastly, the height was constrained using the average estimated height in a certain area. It was seen that the error decreases slightly with the increase of the area size.

Preface

This report is the final deliverable in order to complete my master graduation project and acquire the title of Master of Science in Electrical Engineering. The project was done in association with the Circuits and Systems (CAS) Group, which is part of the Faculty of Electrical Engineering, Mathematics and Computer Science of the Delft University of Technology. The project ran from November 2021 to June 2022, for a total of eight months work.

This project is associated with numerous other projects within the group, with them together making up one of the focus points of the CAS group called Atrial Fingerprinting, which aims to study and derive information from the heart and the cardiac tissue, in order to understand the various disorders that can affect the behaviour of the heart and their underlying causes and mechanisms.

First, I would like to thank Richard Hendriks for his role as project supervisor and Miao Sun as my daily supervisor. You both stayed deeply involved over the course of the project and gave me a great deal of insight and guidance in order for me to complete the project to a success.

Secondly, I would like to show my appreciation to all the people who worked on projects related to Atrial Fingerprinting before me, whose work makes up the foundation of this project and provided me with insight and inspiration.

I would also like to thank my parents for continuously supporting me with my studies and life in general.

Lastly, I also want to thank all of my friends, in particular those who I have worked alongside with during my studies, for bringing me so much joy and helping me through the toughest of times.

Cees H. Kos
Delft, June 2022

Contents

Abstract iii

Preface v

Nomenclature ix

1 Introduction 1

2 Background information 3
2.1 Physiology. . . . 3
2.1.1 Structural overview . . . 3
2.1.2 The cardiac cycle . . . 3
2.1.3 Electrical activity of the heart . . . 3
2.1.4 Measuring the electrical activity of the heart . . . 4
2.1.5 Atrial fibrillation . . . 6
2.1.6 Electrogram analysis . . . 8
2.2 Models. . . . 9
2.2.1 Cell behaviour and models . . . 9
2.2.2 Action potential model . . . 10
2.2.3 Monodomain and bidomain . . . 11
2.2.4 Electrogram model . . . 12
2.3 Ventricular activity removal . . . 13
2.3.1 Categories . . . 14
2.3.2 State of the art . . . 14
2.4 Conductivity estimation . . . 15
2.4.1 Compact matrix model . . . 15
2.4.2 Simultaneous Confirmatory Factor Analysis . . . 16

3 The effects of the sensor-to-cell height on the electrogram, block detection and conductivity estimation 19
3.1 Effect on the electrogram model . . . 19
3.2 Effect on conduction block detection . . . 20
3.2.1 Deriving a conduction block detector . . . 20
3.2.2 Performance of the block detector . . . 23
3.3 Effect on conductivity estimation for varying block size and block strength . . . 23

4 The effects of sensor-to-cell height estimation errors on the electrogram, block detection and conductivity estimation 29
4.1 Effect on the electrogram model . . . 29
4.2 Effect on the performance of the block detector . . . 31
4.3 Effect on conductivity estimation . . . 31

5 Sensor-to-cell height estimation 33
5.1 Problem analysis . . . 33
5.2 Results . . . 38
5.2.1 Height estimation . . . 38
5.2.2 Joint conductivity and height estimation . . . 40
5.2.3 Performance with estimated height versus assumed height . . . 40

6 Conclusion 43

References 45

Nomenclature

Abbreviations

Abbreviation	Definition
SA	sinoatrial
AV	atrioventricular
AP	action potential
ECG/EKG	electrocardiogram
EGM	electrogram
AF	atrial fibrillation
AT	activation time
LAT	local activation time
AM	activation map
CV	conduction velocity
VA	ventricular activity
AA	atrial activity
TMS	Template Matching and Subtraction
AVC	Adaptive Ventricular Cancellation
ICA	Independent Component Analysis
LRSD	Low-rank Sparse Decomposition
ADMM	Alternating Descent Method of Multipliers
GAE	Graph-based Atrial Activity Extraction
CMM	Compact Matrix Model
CPSDM	Cross-power power spectral density matrix
CFA	Confirmatory Factor Analysis
SCFA	Simultaneous confirmatory factor analysis
SNR	Signal-to-noise ratio
GLRT	Generalised Likelihood Ratio Test
MPE	Minimum probability of error
ROC	Region of convergence
FWHM	Full Width at Half Maximum
MSE	Mean square error

1 Introduction

The heart is one of our vital organs, with pumping blood through the body as its main function. Specifically, it pumps oxygenated blood from the lungs to the rest of the body and deoxygenated blood the other way around. The heart functions by periodically contracting in a specific pattern, giving rise to a characteristic rhythmic behaviour. A single contraction is called a heartbeat, with the amount of contractions per time unit being the heart rate, often measured in beats per minute (bpm). Depending on the person and context, this heart rate can be fast or slow, but generally, all hearts show a likewise periodic and rhythmic behaviour.

It can occur, however, that this rhythmic behaviour is distorted, disrupted or otherwise affected. Abnormalities in the heart tissue can cause the heart to behave irregularly. This is because the rhythmic behaviour is governed by electrical signals, which are generated by the heart itself. The electrical signals propagate across the heart in a certain fixed manner, specifically from the top-right to the bottom-left of the heart. As these signals propagate across the heart, they activate the cardiac muscle tissue, which contracts as a consequence.

Abnormalities in the tissue might present themselves as areas of reduced conductivity. A reduction in the tissue conductivity can alter the electrical pathways of the tissue, which causes changes in the rhythmic behaviour of the heart. These conditions are consequently referred to as cardiac arrhythmias.

Cardiac arrhythmias can be caused by several means, including viral infections and hormonal instabilities like thyroitoxycosis [1]. Arrhythmias can be classified based on how regularly they occur, how they affect the heart rate, and their origin. Of the several types of cardiac arrhythmia, one will be of specific interest in this thesis, which is atrial fibrillation (AF). As the name suggests, this set of arrhythmias originates from disruptions of the electrical activity located in the atrial tissue of the heart.

AF can be categorised by its duration [2]. The first category is paroxysmal, in which the AF terminates on its own within seven days. The second is persistent, in which the AF terminates after seven days or has to be terminated by means of pharmacological or direct current cardioversion, meaning an electrical reset of the heart. The third is long-standing persistent, similar to persistent with a duration of more than twelve months. Lastly, there is permanent AF, which remains indefinitely.

Cardiac arrhythmias, like AF, can potentially be fatal. Specifically, AF can result a five-fold risk of a stroke [3], making it the most common cause of embolisms or blood clots [2], of which around 75% end up in the brain area. It is also the most common cardiovascular disease and age-related arrhythmia, presenting itself in 1-3% of the world population [2]. AF is mostly seen in elderly people and is found to be a major cause of morbidity and mortality in this group. This fact that it presents itself in 15% of the people with an age above 70, an amount expected to double with each passing decade [4].

To further study AF, methods have been developed to estimate the conductivity of cardiac cells using epicardial electrograms, or EGMs in short. These inverse problems are generally ill-posed due to the low amount of measurements with respect to the large amount of cells. In addition, other parameters besides the conductivity are involved which have to be estimated jointly or assumed otherwise.

The goal of this project is to consider one of these parameters in the EGM model: the sensor-to-cell height. This height is defined as the distance of sensors to the cells with respect to the cellular and sensory grids. Specifically, the goals of this project are to investigate the following questions:

1. What is the effect of the sensor-to-cell height on the EGM measurements, conduction block detection and conductivity estimation?
2. What is the effect of sensor-to-cell height estimation errors on the EGM, conduction block detection and conductivity estimation?
3. How and to what extend can the sensor-to-cell height be estimated?

The structure of the rest of the report is as follows. In Chapter 2, more in-depth background information is provided. The context of the project is more thoroughly explained and related previous research is summarised. Chapter 3 is composed of an analytical study of the effect of the sensor-to-cell height on the EGM model and conductivity estimation within the context of the environment that is generally assumed in prior research. In Chapter 4, the effect of making estimation errors in the height will be analysed and tried to be confirmed by means of experimental data based on simulations. Then, an attempt is made in Chapter 5 to design and implement an algorithm which estimates the sensor-to-cell height in cases where the height is unknown. Finally, the report is finished with some concluding thoughts in Chapter 6.

2

Background information

2.1. Physiology

2.1.1. Structural overview

The heart is one of a person's vital organs. It can be described as a piece of muscular tissue about the size of a person's fist, located slightly to the left of the centre within the upper torso or chest area. The function of the heart is to pump the blood from a person's body through their circulatory systems: the deoxygenated blood from our body to the lungs and the oxygenated blood the other way. The heart therefore plays a key role in supplying a person's body with oxygen.

The heart is, among other kinds, made up of cardiac muscle tissue, which is a kind of muscle unique to the heart. The heart furthermore consists of two upper chambers, the atria, and two two lower chambers, the ventricles. A schematic representation of the heart is given in Fig. 2.1. The atria and ventricles are pockets made out of cardiac muscle tissue that fill up with blood after which they eject it into the circulatory systems. The atria and ventricles can functionally be divided into two disjoint sets of one atrium and ventricle each. One of the sets pumps blood from the body to the lungs and the other does so the other way around.

2.1.2. The cardiac cycle

During the circulatory process, both atria are filled up with blood, with either oxygenated blood from the lungs or deoxygenated blood from the body. The atria then contract and pump the blood into their respective ventricles, which then contract shortly hereafter to pump the blood out of the heart into the body, followed by a short resting period. This set of actions is repeated periodically and is referred to as a single cardiac cycle or heartbeat. The amount of heartbeats within a certain time frame is regarded as a person's heart rate, which is often measured in cycles per minute or beats per minute (bpm). Adult humans are said to have an average cardiac cycle length of around 0.8 s, corresponding with heart rate of 75 bpm [2].

2.1.3. Electrical activity of the heart

The heart is a large muscle, parts of which are activated and contract periodically. The underlying mechanism that 'powers' the heart is a system of cells with a relatively high conductivity that are able to generate and conduct electrical signals, similar to the way neurons propagate neural signals. Special cells on the heart generate electrical pulses, which then spread out to the various regions of the heart over time. As soon as this signal reaches a cell, the cell is activated and contracts. In order to enable for the periodic behaviour of the heart, the electric signals have to follow a certain specifically timed path across the heart.

At the start of each cardiac cycle, an electrical pulse is generated in the sinoatrial (SA) node, which is located on top of the right atrium. The signal then propagates to the left atrium through Bachmann's bundle, and to the atrioventricular (AV) node, located between the atria and ventricles. There, the electric pulse experiences a brief delay, after which it is propagated further down to the ventricles. The delay imposed by the AV node causes the ventricles to contract slightly after the atria. Important to note is that, due to the high conductivity of the cells it consists of, the delay imposed by Bachmann's

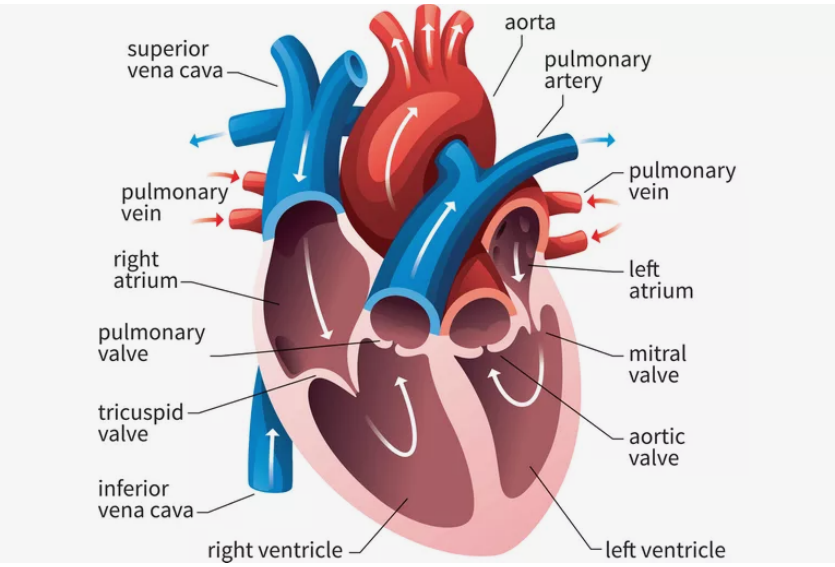

Figure 2.1: Schematic of the structure of the human heart [5].

bundle can be neglected, meaning that both atria effectively contract at the same time. A schematic overview of the heart's main conductive systems is given in Fig. 2.2.

The electrical pulse that propagates across the heart can do so due to the changes in the transmembrane voltages of the cardiac cells. The transmembrane voltage of a single cell over time is referred to as the action potential (AP) of each cell, which has a particularly recognisable shape. The signal starts at its resting potential, followed by a depolarisation of the signal. The depolarisation is followed by a plateau, after which the signal repolarises to the resting potential. An example is shown in Fig. 2.3. After a cell is activated, it takes some time for a cell to be able to activate again. This is called the refractory period. This way of propagation is similar to how signals propagate in and between neural cells. Also, APs measured at different locations on the heart can have different shapes.

2.1.4. Measuring the electrical activity of the heart

There lies a lot of interest in understanding the electrical activity of the heart. Fortunately, there are some ways, one more conventional than the other, to measure and study the electric signals that originate from the heart. Either this is done in a non-invasive way with electrocardiography, or an invasive one called epicardial electrography.

Electrocardiography

Electrocardiography is probably the most popular way to study the electrical activity of the heart. It is a relatively simple method, non-invasive and has no necessary need for expensive equipment.

This method calls for a set of electrodes to be placed upon a person's body surface. These electrodes then measure the electrical signals generated by the heart. The received electrical signal over time is then called an electrocardiogram (ECG or EKG). For official diagnoses, a special configuration is often used called the 12-lead ECG, for which 12 electrodes are placed on the body such that the signals they receive have less correlation, thus yielding a wider range of information on the condition of the heart [1].

The signals received by electrodes often exhibit similar features for each different person, giving the waveform a characteristic shape.

Electrography

Another way of measuring electric signals from the heart is through the use of sensor arrays with high spatial and temporal resolutions, which are placed directly on the surface of the heart during open heart surgery [8]. This method called electrography, exceeds conventional electrocardiography in the sense that the received data, called the electrogram (EGM), provides more detailed information on the more local features of the electrical activity. Due to the high spatio-temporal resolution of the EGM, more

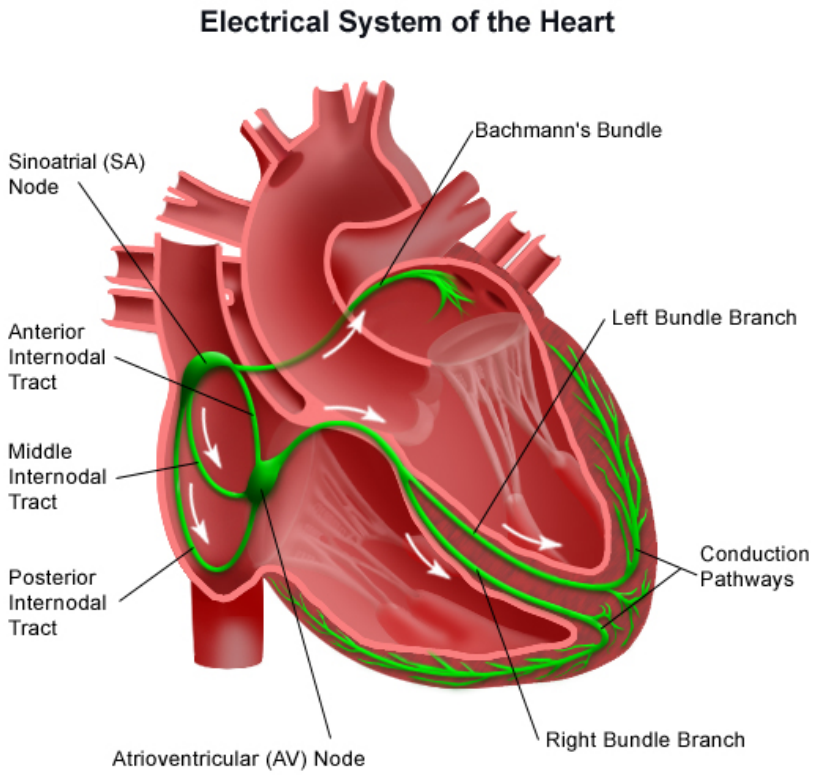

Figure 2.2: Schematic of the electrical conduction system of the human heart [6].

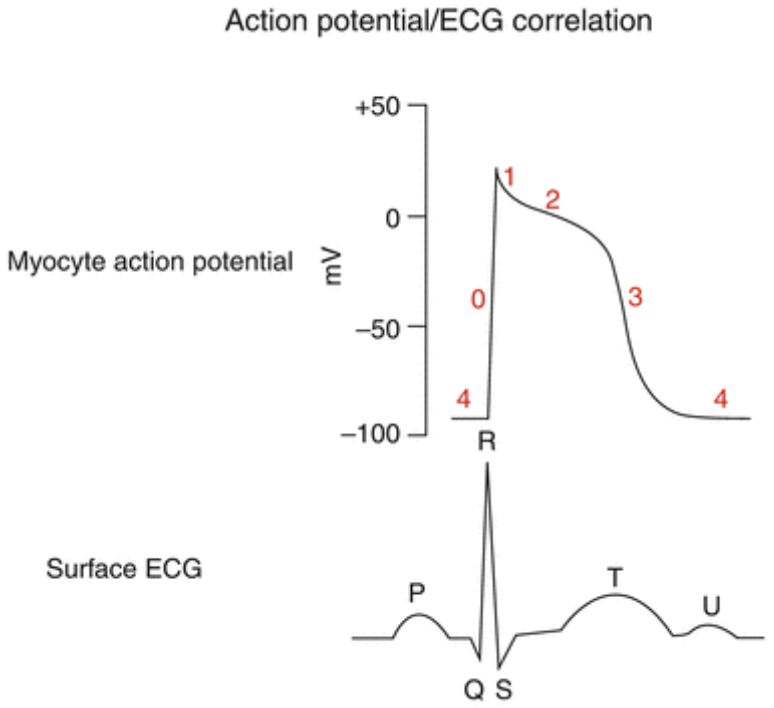

Figure 2.3: Example of a standard atrial AP (top) and ECG (bottom) [7].

information is gathered on particular parts of the heart, as opposed to an ECG, which mostly provides information on the heart as a whole. The process of acquiring EGMs specifically of the atria of the heart is often referred to as atrial mapping.

Although EGMs grant us the possibility of a more in-depth study of the heart, it remains hard to conduct thorough research related to the subject. This is because there is a lack of reference data, due to the fact that EGMs can only be measured under certain conditions during open heart surgery, which is a highly invasive kind of surgery.

The sinus rhythm

As mentioned before, the ECG signals received by electrodes have a certain characteristic behaviour. This is the consequence of each ECG being a sum of the activity of the whole heart over time, thus combining the activity of several regions of the heart. An example of a single cardiac cycle is shown in Fig. 2.3. It is seen that the wave consists of the P-wave, representing the activity in the atria; the QRS-complex, representing the activity during the depolarisation of the ventricles, and the T-wave, representing the repolarisation of the ventricles [2]. This characteristic waveform is referred to as the sinus rhythm of the human heart. Comparing it to the AP of a cardiac cell, see Fig. 2.3, it can be seen how some features of both signals coincide with each other. Deviations from the characteristic waveform often provide important diagnostic information in the detection of heart disorders.

Electrode configurations

With an EGM, more localised information of the electrical activity of the heart is obtained, thus allowing the identification and distinction between signals originating from specific regions of the heart. EGM signals also have a certain shape, represented by a flat line, followed by a sharp peak, a sharp deflection and followed again by a flat line. This is explained by how for a single or unipolar electrode, the potential rises as an electrical pulse or wave approaches an electrode. As the pulse or wave passes the electrode, the polarity of the measured potential flips and the signal decays back to the reference level. A schematic representation of this process is shown in Fig. 2.4a.

As opposed to unipolar measurements, where each measurement site consists of a single electrode, there is also a second configuration referred to as bipolar measurements, which is more commonly used. With this setup, two electrodes are used to measure the potential at a single location. The resulting signal is then taken as the difference between the measurements of the two electrodes, which, if located close enough to each other, can be seen as a high-pass filter or differential operator acting on what would have been the unipolar signal received at the measurement site. The difference between the unipolar signal and its bipolar counterpart is shown in Fig. 2.4b. An advantage of this setup is that the measurements are affected less by any far-field activity, often in the context of far-field ventricular activity affecting local atrial activity. A disadvantage is that the setup is highly dependent on the direction and speed of the incident wavefront. For example, in the case the wavefront propagates in a direction perpendicular to the line of electrodes, no potential would be measured. The distance between the electrodes and the strength distribution of the potential in space can also affect the measurements [2].

2.1.5. Atrial fibrillation

ECGs and EGMs can provide plenty of information on the electrical activity of the heart. This is particularly useful for studying the general behaviour of the heart, as well as for providing information that can be used to identify faults or disorders of the heart related to its electrical activity. These disorders, which are the result of abnormalities in the conductive system of the heart, disrupt the signals that propagate across the heart, causing deviations from its standard rhythmic behaviour. These disorders are referred to as cardiac arrhythmia. These arrhythmias can differ in severity, ranging from totally harmless to outright fatal, the latter case often resulting in things like a blood clot, stroke or cardiac arrest. Cardiac arrhythmias can be caused by several means, including viral infections and hormonal instabilities like thyroitoxycosis [1]. Arrhythmias can also be classified based on how they regularly they occur, how they affect the heart rate, and their origin. Of the several types of cardiac arrhythmia, one kind will be of interest, called atrial fibrillation (AF). As the name would suggest, this set of arrhythmias finds it origin in disruptions of the electrical activity located near the atria.

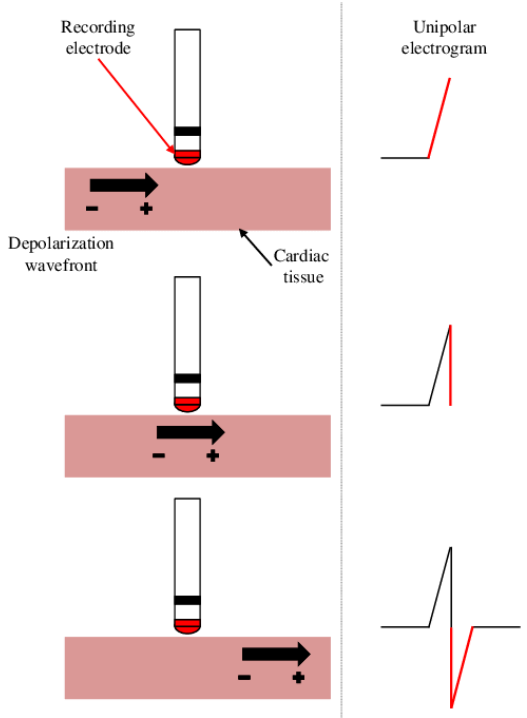

(a) Example of an EGM waveform generated by an electrical pulse passing a unipolar electrode [9].

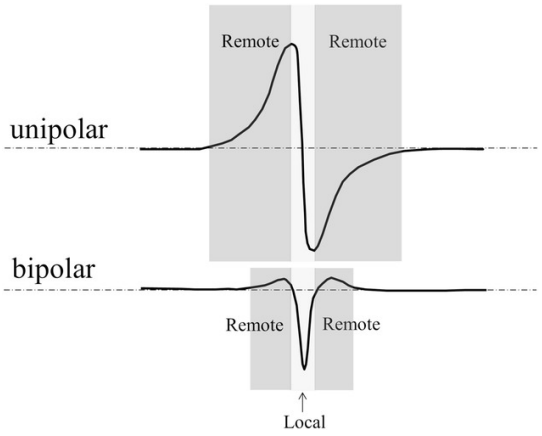

(b) Schematic example of the difference between unipolar and bipolar measurements [10].

Figure 2.4: Schematic representations of (a) how unipolar electrograms are measured and (b) the difference between unipolar and bipolar measurements.

Categories

AF is often categorised based on how long it persists within a patient. Herein, there are four categories: paroxysmal, in which the AF terminates on its own within seven days; persistent, in which the AF terminates after seven days or has to be terminated by means of pharmacological or direct current cardioversion, meaning an electrical reset of the heart; long-standing persistent, similar to persistent with a duration of more than twelve months, and permanent AF [2].

Causes and underlying mechanisms

In the past, people have tried to identify the underlying mechanisms which initiate and maintain AF in the heart. These mechanisms can be seen at different scales. On a larger scale, AF seems to be correlated with the rapid firing of electrical pulses from the pulmanory veins of the heart, as well as with increased amounts of fibrous tissue and enlarged atria. On a much smaller scale, the mechanisms are related to the way the electrical signals are propagated through tissue. Due to the spatial organisation of the tissue, abnormalities in the signal propagation are introduced in the form of ectopic foci, rotors, reentry of signals, breakthrough from neighbouring tissue layers and the maintenance of multiple short-lived wavelets [2].

Ectopic foci are points in the tissue which spontaneously fire electric signals, which interfere with the sinus rhythm. Reentry is when an electric signal follows a circular path in the tissue in which it fails to die out. Rotors are similar to this as regions of functional reentry, but these are active drivers of AF. Breakthroughs happen when a signal from one tissue layer propagates to another, introducing an aberrant electrical source. As the electrical signals move across the heart, they can break up due to inconsistencies in the tissue. This causes for wavefronts to break up. These wavefronts can interact with each other, and potentially interfere with the electrical pathways of the heart [2].

Development and progression

AF is often associated with cases of fibrosis or abnormal growth of the cardiac muscle tissue. Structural changes in or damage to the cardiac tissue are pointed out to be the initial cause of AF and are represented by areas of slow conductivity or conductivity blocks, or more generally as the impairment

of electrical conduction. These structural changes in the heart are referred to as the electropathology of the heart. AF itself also affects the electropathology of the heart, i.e., resulting in a shortening of the refractory period of cardiac cells. This means that the more time spent in fibrillation, the higher the pulse frequency becomes [2].

All in all it seems that the answer to the problem that is AF lies in analysing the condition of the hearts of people suffering from AF. More specifically, in that of the cells, as well as the electrical properties of those cells. It gives rise to the need of determining the hidden underlying parameters governing the electrical behaviour of these cells, such as the conductivity, anisotropy and heterogeneity of the tissue.

The conductivity of cells is related to their ability to transport charge across the membrane of the cells and can be derived from how an electric potential propagates across the membrane, which in its turn is related to the flow of ions through the cell membrane. The problem of finding the cell parameters is therefore presented as an inverse problem using the data acquired with atrial mapping and is regarded as highly ill-posed, due to the difference between the amount of cells and sensors [2]. This the reason why, up until recently, no suitable methods of solving this problem have been presented yet.

Treatment

There are currently no permanent solutions and cure for AF. The most common way to deal with AF is through the use of medication. In more serious cases, non-surgical methods are used to influence the heart, such as the aforementioned cardioversion, which can be seen as a 'reset' of the heart. Cardioversion has proved to be effective, although it loses its effect over time. Another way, which maintains its effect for a longer time, is through ablation. With ablation, cardiac cells which are thought to be the cause of the AF are burned away, creating scar tissue. Ablation is not a very exact way of dealing with AF, since it is often not clear which cells play a role in AF. Therefore, general ablation techniques have been agreed on to treat the heart like pulmanory veins isolation, AV node ablation, linear ablation and electrogram-guided ablation [2]. Ablation is still not very effective, with the AF returning within five years in around 50% of the cases. More surefire ways of dealing with AF are through surgical means like the use of a pacemaker or through open-heart surgery, although this is generally not preferred due to it being invasive and very intrusive treatments, only to be used in the most severe cases.

2.1.6. Electrogram analysis

ECGs and EGMs both provide a way to obtain information on the electrical activity on the heart, the first giving a more general impression of the heart, whereas the second can provide more local information with a higher resolution. The data acquired from atrial mapping is used to solve for the hidden tissue parameters of the heart.

Atrial mapping

As mentioned before, atrial mapping is described as the use of high resolution sensor arrays to record EGMs on different sites of the heart. These measurements are obtained epicardially e.g. on the outside of the heart, as opposed to measurements performed endocardially, meaning on the inside of the heart. Although these measurements provide high resolution data of the atria, a direct drawback is that the atria can not be measured all at once. Measurements of different sites of the atria have to be obtained sequentially.

However, the measured data needs pre-processing to remove unwanted features that are not of interest and/or distort the desired signal. In previous studies, the raw data was filtered before being used. First, a band-pass filter filters the signal from 0.5 Hz to 400 Hz, and a notch filter was used at 50 Hz to cancel out power-line interference. After that, the data needs to be low-pass filtered to remove baseline wandering and high-pass filtered to remove noise, as well as strong far-field ventricular signals need to be removed [2].

Morphology

A lot of information can be gathered from the EGM data and its morphology i.e. the beat-to-beat interval of signals, the number of deflections present in the signal, the amount of symmetry and the amplitude distribution of the wave.

The beat-to-beat interval of waves is dependent on the presence of AF, as AF increases the heart rate and decreases the refractory period. The number of deflections increases due to heterogeneities

in the tissue, possibly indicating slow conduction zones or conduction blocks. Asymmetry of a wave can give an indication of how different wavefronts interfere and interact with each other at a certain location [2], [11]. The wave amplitude varies overall, depending on the complexity of the tissue [2].

Measures

To provide clearer information on the electrical activity measured by the sensor array during atrial mapping, different measures have been defined for the EGM signals. Firstly, the activation time (AT) or local activation time (LAT) of a cell is the instant at which the wavefront reaches a cell, defined as the steepest deflection in the EGM. This gives us an estimate of the LAT of cells directly underneath the sensors, with other ATs being estimated through interpolation. Often, the ATs of all cells in a certain area are presented as an image of the area, providing an activation map (AM) of that area. Secondly, using the ATs of the cells, a measure of the speed with which the wavefront propagates across the tissue can be approximated by taking the difference of the ATs of neighbouring cells and the intercellular distance and dividing them with each other. This measure is called the conduction velocity (CV). Other measures of EGMs include the number of deflections or amount of fractionisation and the peak-to-peak amplitude of the wave [2].

These measures are nowadays primarily used to identify the electropathology of the heart. The CV map is used to identify slow conduction areas and conduction blocks. The CVs however do not give a clear representation of the conductivity of the underlying cells. This is because the CV does not solely depend on the cell conductivity, but on the curvature of the wavefront as well. Specifically, a concave wavefronts propagates faster than convex wavefronts. In addition, the CV map is derived directly from the AM of the cells in a certain area, which is already derived as an interpolated approximation of the true AM. This non-proportionality of the conductivity with respect to the CV requires the intervention of specialists, mainly cardiologists, in order to derive any conclusions from the data. This raises the desire to develop methods to find the underlying parameters of the individual cells directly, as opposed to using the previously mentioned measures derived from the measured data.

2.2. Models

The EGM gives us a lot of information on the electrical activity of the heart, however most of the conclusions are drawn based on derived measures of the measured data. The desire arises to acquire the hidden underlying parameters of the tissue, in order to give direct knowledge of the tissue. These parameters include, but are not limited to, the conductivities and conductivity anisotropy ratios of cells, and their ATs for a set of measurements. It is herein important to analyse what parameters are of importance to the electrical activity of the heart and how they relate to the data that we measure, the EGMs. Since there is a lack of clinical reference, suitable testing environments need to be used as well, which require tissue models that are able to represent real data.

2.2.1. Cell behaviour and models

Developing a realistic model of cells of interest is of great importance in finding the underlying parameters thereof, as there is a lack of labelled clinical data to test new solutions. In the past, a lot of research has been done into the behaviour of the cells of different kinds, among which cardiac cells, and the underlying mechanisms responsible for its behaviour [12]. Most of these models are based on the research done by Hodgkin and Huxley, who studied the propagation of electric potentials in the axons of a giant squid [13], [14], [15], [16]. Through this, they gained important insight into the electrodynamic behaviour of the axon, and also found that the propagation of a potential across cells depends on how different kinds of ions move through the cell membrane over time. Inferring the individual contribution of each ion current to the propagation of an electric pulse where it is given that there is a larger amount of sources than receivers, which is the case for atrial mapping, is an undetermined and ill-posed problem, which also affects the accuracy of the estimation of any other hidden parameters. By studying the relationship between the ion currents and the transmembrane voltage of the neural cells, they were able to describe them using different sets of differential equations for both the transmembrane voltage of a cell and the individual ionic currents. Using this knowledge, different models were designed. Over time, the knowledge on the electrical behaviour of cells was expanded with the identification of more and more different machinations that define the dynamic behaviour of cells, resulting in more complex models, such as the Courtemanche model for the single atrial cell [17].

To study the propagation of signals across cells, studies have been performed in different contexts in terms of dimensionality. At first, the behaviour of cells in 1D was considered by studying electrical propagation in terms of the CV in strands of cardiac tissue [18]. This was then extended to the 2D case, where anisotropy and curvature of the wavefront started to play a role and complicate the relationship between the conductivity and CV [19]. Recently, the 3D AP propagation case has been considered, in which the structure of the tissue becomes more important. The heart tissue is then said to have a fibre-sheet structure in which different layers can influence the neighbouring ones [20], [21], [22].

For simulations of cell models, 2D models are used to represent 3D tissue. 1D models lack the diffusive spatial component, whereas 3D models are too involved in terms of analytical and computational complexity. The use of 2D models provides a good compromise, its only drawback being that it can not represent 3D tissue in the sense that it does not take the interactions between multiple tissue layers into account, which is the case in real-life [20], [22].

For models of biological tissue, some important statements can be made. It is important to note that models are often very limited in the kind of data that they can process and produce. This arises a necessity for separate models to be developed for different kinds of cells and tissue to maintain accuracy. It is also good to consider how the model represents reality and in what ways it might be possible to fix any degrees of freedom. For example, it is often assumed that the type of cells is known, as well as the heart being homogeneous in the type of cells. Whatever assumptions are made when making a model, it is good to consider what kind of effect certain assumptions can have on its output. Within the context of creating a model representing biological tissue, of which certain parameters are to be studied, it is necessary to include them in the model as well as parameters to have a direct reference. It is advised to well take any natural tendencies of a model into mind. An example of this is that for heart tissue models, there exists the diffusive current, which removes energy from the modelled system. If by chance the input energy is too small, the model might not work. In practice, this means that a minimal part of the model needs to be exited for the model to show any output. This is referred to as the liminal length, area or volume for 1D, 2D and 3D models respectively [20].

2.2.2. Action potential model

Over time, different models for different kinds of cells were introduced, with making the models more realistic and able to simulate real-life data as their goal. The models of cardiac cells are largely based on the equations describing the propagation of an AP across the cell membrane as described by Hodgkin and Huxley, who used in their experiments the axon of a neuron in a giant squid. In their experiments, they did not only manage to give descriptions of and relations between the transmembrane voltage and the underlying ionic currents using differential equations, but also showed the behaviour of the transmembrane conductances for each type of current over time.

Hodgkin and Huxley found that the transmembrane voltage depends on the ionic currents that flow through the membrane, which again depend on the concentrations of ions inside and outside of the cell [13], [14], [15], [16]. Aside from these concentration-dependent ionic currents, there flows a capacitive current due to the difference in amount of charge on both sides of the cell membrane. Potentially, a cell can be stimulated with a current source from the outside. A circuit model representation of the cell membrane is given in Fig. 2.5.

The behaviour of the transmembrane voltage over time is then given as a differential equation by

$$C_m \frac{\partial V(t)}{\partial t} = I_{st}(t) - I_{ion}(t, V), \tag{2.1}$$

where C_m is the transmembrane capacitance, V is the transmembrane voltage, I_{st} and I_{ion} are the stimulation and total ionic current densities, respectively, and t denotes the time. For modelling multiple cells, a term is added to (2.1) to describe the current caused by spatial voltage differences, turning it into

$$C \frac{\partial V(\mathbf{r}, t)}{\partial t} = I_{tm}(\mathbf{r}, t) + I_{st}(\mathbf{r}, t) - I_{ion}(\mathbf{r}, t, V), \tag{2.2}$$

where I_{tm} represents the so-called transmembrane or diffusive current and $\mathbf{r}$ is the location on the membrane. Using the monodomain approach, this transmembrane current is given as

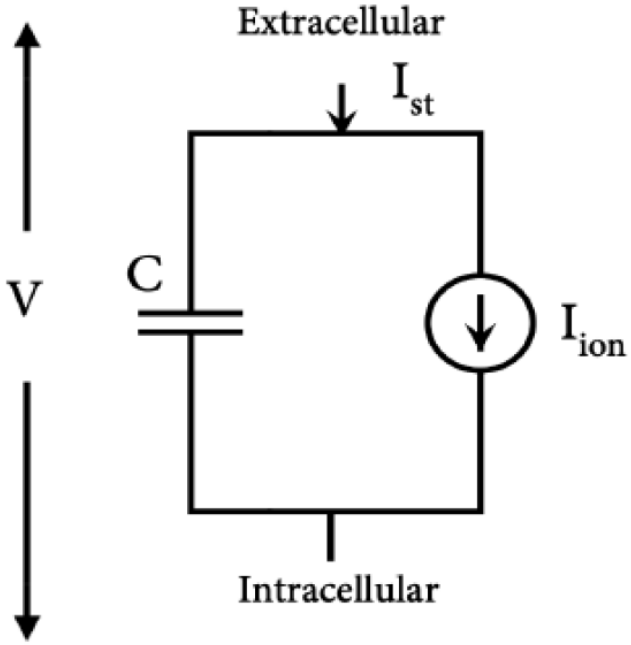

Figure 2.5: Circuit model of a cell membrane [2].

$$I_{tm}(\mathbf{r},t) = S_v^{-1}\nabla\cdot(\Sigma(\mathbf{r})\nabla V(\mathbf{r},t)), \tag{2.3}$$

where $S_v = 0.24\,\mu\text{m}^{-1}$ is the surface-to-volume ratio of the cell and $\Sigma(\mathbf{r})$ is a conductivity tensor defined in the 2D case as

$$\Sigma(\mathbf{r}) = \begin{bmatrix}\sigma_{xx} & \sigma_{xy}\\ \sigma_{xy} & \sigma_{yy}\end{bmatrix}, \tag{2.4}$$

where each conductivity σ_{ij} describes the propagation into the main directions of the spatial grid. For simplicity, a cell is often described as it having a longitudinal or main direction and an orthogonal or transverse direction, and having a certain orientation. The ratio between the conductivity in the main direction and the transverse direction is then called the anisotropy.

2.2.3. Monodomain and bidomain

The term monodomain describes the relation between the inside and outside of the cell. When prepared to activate, cardiac cells show cable-like properties [21]. Heart tissue can therefore be modelled as an extracellular and intracellular domain, divided by the cell membrane. In general, these two domains have a different structure and electric signals propagate differently within the two domains with respect to each other. This can be modelled by using different conductivity sensors for both domains. The relationship between the two domains through the transmembrane current is then described as

$$\nabla\cdot(\Sigma_i(\mathbf{r})\nabla\phi_i(\mathbf{r},t)) = S_v I_m(\mathbf{r},t) \tag{2.5}$$
$$\nabla\cdot(\Sigma_e(\mathbf{r})\nabla\phi_e(\mathbf{r},t)) = -S_v I_m(\mathbf{r},t), \tag{2.6}$$

where ϕ_i and ϕ_e denote the intracellular and extracellular potentials. The cell membrane model is in this case described by

$$C_m \frac{\partial V(\mathbf{r},t)}{\partial t} = S_v^{-1} \nabla \cdot (\Sigma_i(\mathbf{r}) \nabla (V(\mathbf{r},t)) + \phi_e(\mathbf{r},t))) + I_{st}(\mathbf{r},t) - I_{ion}(\mathbf{r},t,V) \tag{2.7}$$

$$\nabla \cdot (\Sigma_i(\mathbf{r}) \nabla \phi_i(\mathbf{r},t)) = -\nabla \cdot (\Sigma_e(\mathbf{r}) \nabla \phi_e(\mathbf{r},t)). \tag{2.8}$$

This is called the bidomain approach [23], [24], [25]. The equations can be solved for the transmembrane voltage using methods such as Euler's method with boundary constraints. The drawback of the bidomain approach is that the extracellular potential has to be solved implicitly. To simplify the model, it can be assumed that the intracellular and extracellular domain have the same anisotropy, which is the ratio between the conductivity in the main direction and the transverse direction of a cell, and consequently that they are related as

$$\Sigma_i(\mathbf{r}) = c\Sigma_e(\mathbf{r}), c > 0, \tag{2.9}$$

which is substituted into the bidomain model [24]. By also grounding the extracellular potential, this results in the monodomain model as described by (2.2) and (2.3). An advantage of using the monodomain approach is that it can be solved explicitly and uses less parameters. Disadvantages are that it ignores the fact that some currents can only be described in the bidomain model and that influences from the outside, like defribillation or pacing, are not taken into account. It is still argued that the monodomain provides an accurate enough model if used in a less complex context.

2.2.4. Electrogram model

Heart cells can be modelled as a conductive surface across which electrical pulses propagate through changes in the transmembrane voltage of cells and the electrodynamic interactions between them. These signals can be measured as they propagate across a certain surface as EGMs with atrial mapping. A sensor at a certain point in space measures the signals originating from nearby cells, weighted depending on how far they are removed from the sensor.

Continuous model

The electrical potential measured by a sensor m positioned at location $\mathbf{r}_m \in \mathbb{R}^2$ at time t can be modelled as [1], [2], [26], [27].

$$\phi_m(\mathbf{r}_m,t) = \frac{1}{4\pi\sigma_e} \int_{\mathcal{A}} \frac{I_{tm}(\mathbf{r},t)}{||\mathbf{r}_m - \mathbf{r}||} \mathrm{d}A(\mathbf{r}), \tag{2.10}$$

where $\mathcal{A}$ represents the region of interest, σ_e is the extracellular conductivity, which is assumed to be constant and known, I_{tm} is the transmembrane current as given in (2.3), $\mathbf{r} \in \mathbb{R}^3$ denotes a location on the tissue surface and $||\cdot||$ represents the Euclidean norm. An interesting observation here is that the model resembles a 2D spatial convolution, with the signals coming from the cells going through a spatial low-pass filter.

Discrete model

In practice, a finite space-discretised version of this model is used. Consider a set of M sensors positioned at locations $\mathbf{r}_m \in \mathbb{R}^3, m \in [1,2,...,M]$. The region of interest is then divided into N discrete cells or cell groups with location $\mathbf{r}_n \in \mathbb{R}^3, n \in [1,2,...,N]$, with each cell or cell group having an surface area a. The 2D space-discretised version of (2.10) can then be written as

$$\phi_m(\mathbf{r}_m,t) = \frac{a}{4\pi\sigma_e} \sum_{n=1}^{N} \frac{I_{tm}(\mathbf{r}_n,t)}{r_{m,n}}, \tag{2.11}$$

The above model holds for, but is not restricted to, the 2D case, as a similar mathematical model can also be derived for the 3D case. In the 2D case, the sensors and cells are assumed to be situated on two parallel planes, therefore fixing the orthogonal distance, or height, z_0 between them. The distance between a sensor m and cell n is then calculated as

$$r_{m,n} = \sqrt{||\mathbf{r}_m - \mathbf{r}_n|| + z_0^2}. \tag{2.12}$$

The transmembrane current is also discretised and consequently given as

$$I_{tm}(\mathbf{r}, t) = S_v^{-1} \nabla \cdot (\Sigma(\mathbf{r}_n) \nabla V(\mathbf{r}_n, t)) \tag{2.13}$$

$$\begin{aligned} &= S_v^{-1} \left(\frac{d}{dx} \left(\sigma_{xx,n} \frac{dV(\mathbf{r}_n, t)}{dx} \right) + \frac{d}{dx} \left(\sigma_{xy,n} \frac{dV(\mathbf{r}_n, t)}{dy} \right) \right. \\ &\quad \left. + \frac{d}{dy} \left(\sigma_{yx,n} \frac{dV(\mathbf{r}_n, t)}{dx} \right) + \frac{d}{dy} \left(\sigma_{yy,n} \frac{dV(\mathbf{r}_n, t)}{dy} \right) \right) \end{aligned} \tag{2.14}$$

Action potential template
To simplify the model further, it is often assumed that when a cell is activated, the transmembrane voltage has the same waveform for each cell [2], [26]. This means that the transmembrane voltages $V(\mathbf{r}_n, t)$ for each cell can be modelled as a template waveform $V_0(t)$ that is delayed by the activation time τ_n of each cell as

$$V(\mathbf{r}_n, t) = V_0(t - \tau_n) \tag{2.15}$$

Electrode size
What is not yet included in the model, is the effect of the electrode. Previously, the electrode or measurement location was considered to be a single point. In reality, this is not the case, and at a certain point, the diameter of the electrode has to be taken into account. In general, the potential measured at a sensor m can be modelled as the convolution of the signals that originate from the cells with a spatial low pass filter multiplied by a constant, and is given as

$$\phi_m(r, t) = cI_{tm}(r, t) * R_0(r, t) \tag{2.16}$$

where $c = \frac{a}{4\pi\sigma_e}$ is the constant term from (2.11), I_{tm} represents the transmembrame current signals of the cells, R_0 is the spatial low-pass filter and $*$ represents a 2D spatial convolution. The spatial low-pass filter for a given constant height z_0 is given as

$$R_0(r, t) = \frac{1}{\sqrt{r^2 + z_0^2}} \tag{2.17}$$

where $r = \sqrt{x^2 + y^2}$ is the distance between the cell and the electrode, with the electrode being located at the origin. It is stated that, once an electrode has a diameter d_0 larger than the size of one cell, the electrode can no longer be considered as a single point and therefore has to be taken into account in the transfer function, which then takes the form as seen in [2], [28]

$$R_{d_0} = 2 \arcsin \frac{d_0}{\sqrt{(r - d_0/2)^2 + z_0^2} + \sqrt{(r + d_0/2)^2 + z_0^2}} \tag{2.18}$$

2.3. Ventricular activity removal

As mentioned before, the data recorded by the sensor array needs to be pre-processed before it can be used. Part of this included applying several filters to remove unwanted signal features like baseline wandering and noise. The second part includes removing components resulting from far-field ventricular activity (VA) that interferes with the local atrial activity (AA) in the case for performing measurements of the atria [2], [29], [30]. The presence of these far-field components is seen as a liability since the ventricular activity is much stronger and more present than the atrial activity. For a normally functioning

heart, the ventricles and atria are active at different points in time, with the ventricles always contracting slightly after the atria. This means that normally, the interference is not a big problem. The need to remove any ventricular activity arises more often in cases of atrial fibrillation. Atrial fibrillation describes irregular atrial electrical activity. This can lead to situations where atrial activity coincides with ventricular activity. Not only do the AA and VA overlap in time, but in frequency as well. Also, the AA and VA are depend on and are correlated with each other, since they both originate from the rhythmic behaviour of the heart. Since it is still desired to study the atrial activity on its own, the local and far-field activities need to be separated.

2.3.1. Categories

There are a number of base categories of methods that have been identified in the past, all of which will be discussed next.

Template Matching and Subtraction

One of the most simple methods is that of Template Matching and Subtraction (TMS) [2], [3], [4]. TMS makes use of the spatio-temporal alignment of the QRS complex of separate heartbeats. For this method, a large amount of data is used to compute a template for the average heartbeat signal, similar to the to-be-processed signal. This template is then subtracted from the signal, leaving only the irregular atrial activity. This method works with the assumption that AA and VA have no fixed correlation and that VA has no fixed morphology. This implies that this method achieves a high performance on average, which is seen in the fact that it achieves the highest performance for disorganised AA.

Adaptive Ventricular Cancellation

Adaptive Ventricular Cancellation (AVC) tries to estimate the underlying VA from the data using a template VA signal [2], [3], [4]. By iterating over an adaptive filter based on the difference between the template and estimate signals, an estimate for the VA is constructed and subtracted from the signal of interest. Although AVC tries to confront the signal with an estimate, previous works state that AVC has the worst performance of all base categories of methods.

Independent Component Analysis

Independent Component Analysis (ICA) is based on performing Blind Signal Separation (BSS) on the data to separate the AA and VA [2], [3], [4]. From all base categories, this method achieves the highest performance for organised AA.

2.3.2. State of the art

Extending from the above categories, recently, new methods have been introduced to remove VA.

Low-rank Sparse Decomposition

Abdi [2], [29] proposed a method called Low-Rank Sparse Decomposition (LRSD). With this method, first the VA containing segments of the measured data are put into a matrix. This method optimises for the AA and VA under the assumption that VA activity has a low rank in the time domain, due to having a similar morphology at different locations, is sparse in the frequency domain, as it is often represented by a smooth and slow signal, and that AA is random and sparse in time. An optimisation problem is solved accordingly using the Alternating Descent Method of Multipliers (ADMM), resulting in estimates for the separated AA and VA. The advantages of this method present itself in its low complexity, the fact that it requires no form of calibration and that it outperforms all previously mentioned methods. A disadvantage that is pointed out is that, as a smaller amount of VA segments becomes available, the Singular Eigenvalue Decomposition used to separate the AA from the VA becomes less accurate, resulting in AA activity being removed as well. Another limitation of this method is found in the fact that it uses only a single recording at a time, therefore using no spatial information.

Graph-based Atrial Activity Extraction

Later on, Sun [30] proposed a method called Graph-based Atrial Activity Extraction (GAE). This method includes the spatial information that was missing from the aforementioned methods, by modelling the tissue as a graph, as opposed to a grid. It was found that VA resides in the lower spatial frequencies of the graph. By using this information in addition to the time-frequency analysis, The VA

was estimated by minimizing the distortion of the VA with the measured EGM and by reconstructing the VA as a smooth graph signal.

2.4. Conductivity estimation

Cardiac arrhythmia are disorders affecting the rhythmic behaviour of the heart. One of those disorders is called atrial fibrillation or AF in short, which finds its cause specifically in the upper chambers, the atria, of the heart. The cause of AF is thought to be abnormalities in the conductivity of the heart tissue. In other words, the manner in which it propagates the electrical pulses that drive the heart's function. The need arises to think of solutions for estimating the hidden tissue parameters of the heart. Recently, some works were published which address the conductivity estimation problem and introduced some methods to do as such.

2.4.1. Compact matrix model

Abdi [2], [31] presented a method called the compact matrix model (CMM). The desire was to derive a model for the measured data which was linearly dependent on the parameters of interest i.e. the conductivities of the individual heart cells. In this work, such an expression was derived and given by

$$\boldsymbol{\phi} = \mathbf{M}_\tau \boldsymbol{\sigma}, \tag{2.19}$$

where $\boldsymbol{\phi}$ is a vector containing all measurements in space and time, $\mathbf{M}_\tau$ is the derived linear transformation matrix model and $\boldsymbol{\sigma}$ is a vector containing the conductivities of all cells. Since $\mathbf{M}_\tau$ is non-invertible, the problem was solved as an optimisation problem. To combat the ill-posed nature of the problem, regularisation terms were added, resulting in the optimisation problem given as

$$\min_{\sigma} J(\sigma) = ||\boldsymbol{\phi} - \mathbf{M}_\tau \boldsymbol{\sigma}||_2^2 + \lambda_1 ||\boldsymbol{\sigma} - \mu_\sigma \mathbf{1}||_1 + \lambda_2 ||\Sigma - \mu_\sigma \mathbf{1}\mathbf{1}^T||_* \tag{2.20}$$

where μ_σ is the expected average value of the tissue conductivity, Σ is a matrix containing all cell conductivities, λ_1 and λ_2 denote penalisation parameters, and $||\cdot||_*$ denotes the nuclear norm. the L1-norm is used to promote the sparsity in the conduction map as an aid to the detection of conduction blocks. The nuclear norm is there to do the opposite and try to make the conductivity values vary smoothly around an expected average value. This is done based on the assumption that for normal tissue, the conductivity map exhibits this smooth behaviour. The proposed optimisation problem was then solved using an algorithm called the Split-Bregman algorithm.

In order to estimate the conductivity in this way, it is assumed that the ATs of the cells or estimated or otherwise known. The ATs of cells directly below the EGM sensors are estimated by taking the time of the steepest descent in the EGM signal. The ATs of other cells are then derived through interpolation. However, in the case of less smooth wavefronts, more heterogeneous tissue and the presence of blocks, EGM might also record local deflections. This raises the chance of making errors in the LAT estimation. To overcome this, Abdi [2], [11], [32] also proposed an optimisation problem that optimises for the diffusion current signals from the individual cells. This should remove any local deflections and give more accurate LAT estimations. To estimate the diffusion currents, the optimisation problem is given by

$$\min_{\mathbf{i}} ||\mathbf{D}_t \mathbf{i}||_1 + \lambda ||\boldsymbol{\phi} - \mathbf{S}\mathbf{R}\mathbf{i}||_2^2 \tag{2.21}$$

where $\mathbf{D}_t$ denotes the time differentiation operator, $\boldsymbol{\phi}$ is the vector holding all measurements, $\mathbf{S}$ is a masking matrix selecting the locations of the sensors, $\mathbf{R}$ is the convolution matrix of the spatial low-pass filter and $\mathbf{i}$ is a vector holding all the diffusion current values for all cells. The LAT was then to be estimated as the time of the steepest descent in each diffusion current signal. It was shown that by using this method, there was a significant decrease in LAT estimation errors, and tests showed it outperformed all other LAT estimation methods as well. This new method of LAT estimation is also said to be more computationally efficient, has less of a performance decrease due to boundary effects and can operate with incomplete measurements data.

There are a few disadvantages to this method. The first is that it assumes a constant sensor-to-cell height. The second is that it does not take into account the thickness of the tissue and the shape of the wavefront. All of the above assumptions have an impact on the shape of the wave and therefore on the LAT estimation as well.

As far as the CMM goes, a few recommendations were made. For one, the CMM depends on good estimation of the ATs of the cells and on the validity of the measured data. It also has a decrease in performance in the case of a non-smooth wavefront, in which case a better LAT estimation is desired. The method is also based on the 2D convolution model and can therefore not be used in a 3D context. In that case, the method would require a 3D activation map, for which there are no methods of constructing one as of yet. In her work, Abdi also did not focus entirely on choosing the most optimal parameters in the optimisation problem, which leaves room for improvement. Then, an important disadvantage, is that the CMM method only works with one heartbeat, whereas more information can be acquired by including the possibility of multiple heartbeats per EGM measurement.

2.4.2. Simultaneous Confirmatory Factor Analysis

Shortly after the introduction of the CMM method, Sun [26] introduced a different method for conductivity estimation called simultaneous confirmatory factor analysis (SCFA). This method is based on estimation the hidden parameters of interest from the correlations and cross-power spectral density matrices (CPDSMs) between signals recorded at different locations. To this end, the estimation of the hidden parameters was related to a type of signal modelling called confirmatory factor analysis (CFA), which focusses on finding the values of variance-covariance structures, which then can be related to estimating the power spectral densities of the signals.

CFA has some prerequisites for it to be able to work properly, regarded as the identifiability conditions.

The first identifiability conditions states that there should be more known than unknown parameters. Known parameters include the sensor measurements. Unknown parameters include the conductivities, anisotropy ratios, sensor-to-cell height, fiber directions and ATs of the cells. To simplify the problem, some of the unknowns are assumed to be known and/or estimated through other means. In general, the conductivities are seen as the parameters of interest. The tissue is also either assumed to be isotropic or have some approximate real-life value. The fiber direction is assumed to be constant and directed into one of the grid main dimensions. The ATs are assumed to be known as well.

The second indentifiability condition states that there should be a minimal amount of known parameters. This prevents the system to have an infinitude of solutions. This problem was solved by assuming the same waveform for the transmembrane voltage for every cell.

As said before, the number of knowns is determined by the amount of measured data. This can be increased by both increasing the number of electrodes and the spatial resolution. Increasing the resolution results in a higher accuracy and decreases the model mismatch, but can increase any optimization errors.

After setup, the CFA problem is solved using the interior-point algorithm. It can be seen from earlier work that the performance of this method depends on the ratio between knowns and unknowns. Sun noted that the tissue parameters stay the same at different frequencies. It was then proposed to split the standard CFA problem into multiple sub-problems considering different frequency bands being solved simultaneously. This resulted in the SCFA method as presented at last.

The SCFA method was then compared to the CMM method in their ability to estimate the hidden parameters, which showed that the SCFA shows a significant increase in performance over the CMM method.

As the signals are spatially low-pass filtered due to the distance to the sensors, it was suggested to use the lower frequency bands over higher ones in order to improve performance, since they would hold more information. Naturally, increasing the number of frequency bands also improves the performance, but loses its impact with the amount of used frequency bands. Also, by using more frequency bands, more parameters can be estimated on the same performance levels. This gives the option to include other parameters into the optimisation framework which were assumed to be known before, like the anisotropy ratios and the ATs of the cells. Included in her work, Sun tested this as well, seeing a slight decrease of performance when estimating a larger amount of parameters.

Lastly, the main limitations of the SCFA method still lie in the fact that it only works for a single fiber direction of the tissue and that the method assumes a 2D environment and would possibly lose a

great deal of performance for 3D applications.

In her further work, Sun extended on the SCFA method to include multiple heartbeats per measurement. The idea herein was that the direction of the wavefront changes slightly with every heartbeat, which might give more information on the underlying tissue. The use of multiple heartbeats in this way helps to better estimate the conductivity of the tissue in different directions, which is related to the anisotropy ratio of each cell. Furthermore, the consequences of using multiple heartbeats include the need to estimate the ATs of every cell once for every heartbeat. Despite the follow-up method making less assumptions about the tissue, it still assumes a single fiber direction and a 2D single-layer environment.

3

The effects of the sensor-to-cell height on the electrogram, block detection and conductivity estimation

As mentioned in Chapter 2, the key to understanding the underlying causes and mechanics of AF is to study the cardiac tissue and its properties. The focus is on the cell conductivities, but also can include the orientation and anisotropy of the tissue. In the previously mentioned methods for conductivity estimation, the CMM and SCFA, it is primarily assumed that the tissue consists of a single layer. The individual cells are herein located on a plane, with the sensors being located on a different plane parallel to the cells. A schematic representation of this situation is seen in Fig. 3.1. In the following chapter, the effect of the height as a parameter in the model used for conductivity estimation will be studied. To that end, not only do we take a look at the EGM model itself, but we will also develop a detector with which we will try to explain the effect of all involved parameters on the ability to accurately estimate any parameters of interest.

3.1. Effect on the electrogram model

To start off in a simple way, the effect of changing the distance between the sensors, denoted in Fig. 3.1 as z_0, will be studied to see what kind of effect such changes have on the measured data, the EGMs, and consequently the information about the tissue which can be inferred from it. For this, we will consider again the space-discrete EGM model and the definition of the sensor-to-cell distance from Chapter 3. It can then easily be seen that one simple consequence of increasing the height is a decrease in signal intensity. This will naturally lower the signal-to-noise ratio (SNR) of the EGM with respect

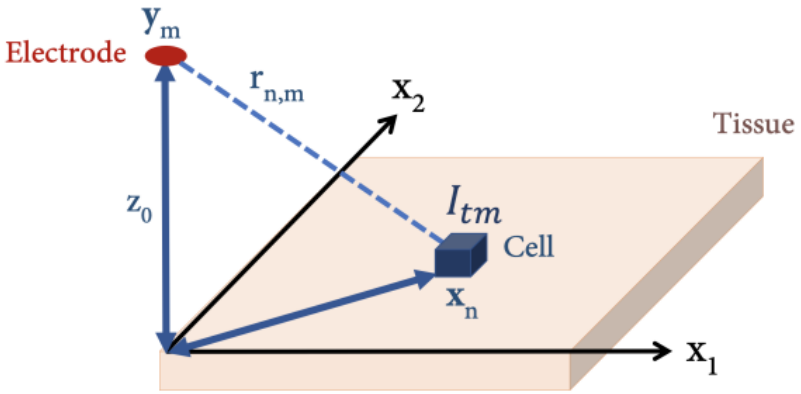

Figure 3.1: Schematic of the single layer tissue model (adapted from [2]).

to any noise added within the measurement system, for example the self-noise of the EGM sensor array. This makes it harder to derive information about the tissue based on the characteristics of the received signal. In addition, a non-zero height also acts as a spatial low-pass filter which smooths and dampens the received signals in space.

3.2. Effect on conduction block detection

3.2.1. Deriving a conduction block detector

To further investigate the effect of a varying height, we will try to approach the problem from a different direction. In general, the inference of information on the cardiac tissue is desired to study AF and its possible causes. Assuming that the AF is mainly caused by conduction blocks and slow conduction zones in the tissue, which disrupt the electropathology of the heart, it is desired to know where those conduction blocks occur in order to treat and deal with them in a correct manner. In short, from measured data, we want to be able to say something about whether certain parts of the cardiac tissue are parts of a block or not.

The idea is to approach this in a stochastic way by building a detector which can decide for any cell whether it belongs to a conduction block or not, given the EGM measurements. For this, some prior information has to be assumed. First, the distributions of the cell conductivities are assumed to be known for both normal tissue and slow conduction zones and blocks. An obvious way to classify the cells into blocks and normal tissue is to to determine from which distributions their conductivity values were drawn. A hypothesis test for determining whether a certain cell of interest c belongs to a conduction block or not can be described as

$$\begin{aligned} \mathcal{H}_1 &: \sigma_c \sim \mathcal{N}(\sigma_{fg}, v) \\ \mathcal{H}_0 &: \sigma_c \sim \mathcal{N}(\sigma_{bg}, v) \end{aligned} \tag{3.1}$$

where σ_c denotes the conductivity of a cell of interest c, σ_{fg} and σ_{bg} denote the expected values for the conductivity of blocks and normal tissue respectively, v denotes the variance of the cell conductivities, which is assumed to be the same for normal tissue and conduction blocks, and $\mathcal{N}(\mu, \sigma^2)$ denotes a normal distribution with expectation μ and variance σ^2. Also important to define are the prior probabilities of a cell belonging to a block or not. These are denoted as P_{fg} and P_{bg} respectively, which are defined as

$$P_{fg} = P(\mathcal{H}_1) \tag{3.2}$$

$$P_{bg} = 1 - P_{fg} = P(\mathcal{H}_0) \tag{3.3}$$

where the subscripts fg and bg of the conductivities in (3.1) and the prior probabilities in (3.2) and (3.3) stand for the foreground or conduction blocks, and the background or normal tissue, respectively.

From one of the aforementioned conductivity estimation methods, the CMM [2], [31], it can be seen that the EGM measurements at all times and locations can be modelled as a linear combination of the cell conductivities of the cardiac tissue as

$$\boldsymbol{\phi} = M_\tau \boldsymbol{\sigma} \tag{3.4}$$

where $\boldsymbol{\phi}$ is the vector containing all measurements in space and time, $\boldsymbol{\sigma}$ the vector of all cell conductivities, and $\mathbf{M}_\tau$ is the mixing matrix from [2], [31], defined as

$$\mathbf{M}_\tau = (\mathbf{V}_\tau^T \otimes (k\mathbf{R}))\boldsymbol{\Gamma} \tag{3.5}$$

where $\mathbf{V}_\tau$ is the matric holding the transmembrane voltages for all cell, k is the constant term of the EGM model from 2, $\mathbf{R}$ is the matrix holding the inverse sensor-to-cell distances, and $\boldsymbol{\Gamma}$ is a matrix holding the conductivities and the spatial derivatives of the conductivity map. The sensor-to-cell diatances are then proportional to the height parameters z, which is of interest to us. The measurement with index i can then be modelled as

$$\phi_i = \sum_{n=1}^{N} [M_\tau]_{i,n} \sigma_n \tag{3.6}$$

In (3.1), normal distributions were assigned to the cell conductivities. It then follows that the EGM measurements can be described with a normal distribution as well and that the test can be rewritten in terms of the measurements ϕ_i as

$$\begin{aligned} \mathcal{H}_1 &: \phi_i \sim \mathcal{N}(\mu_{\phi,1}, v_\phi) \\ \mathcal{H}_0 &: \phi_i \sim \mathcal{N}(\mu_{\phi,0}, v_\phi) \end{aligned} \tag{3.7}$$

with the distribution parameters being defined as

$$\mu_{\phi,1} = \mathrm{E}[\phi_i|\mathcal{H}_1] = [M_\tau]_{i,c}\sigma_{fg} + \sum_{n=1, n\neq c}^{N} [M_\tau]_{i,n}(P_{fg}\sigma_{fg} + P_{bg}\sigma_{bg}) \tag{3.8}$$

$$\mu_{\phi,0} = \mathrm{E}[\phi_i|\mathcal{H}_0] = [M_\tau]_{i,c}\sigma_{bg} + \sum_{n=1, n\neq c}^{N} [M_\tau]_{i,n}(P_{fg}\sigma_{fg} + P_{bg}\sigma_{bg}) \tag{3.9}$$

$$v_\phi = \mathrm{Var}(\phi_i|\mathcal{H}_1) = \mathrm{Var}(\phi_i|\mathcal{H}_0) = v \sum_{n=1}^{N}\sum_{p=1}^{N} \rho_{n,p}[M_\tau]_{i,n}[M_\tau]_{i,p} \tag{3.10}$$

where $\rho_{n,p} \in [-1, 1]$ denotes the correlation coefficient between cells n and p, which is assumed to be known, and the fact is used that

$$\mathrm{E}[\sigma_c|\mathcal{H}_1] = \sigma_{fg} \tag{3.11}$$

$$\mathrm{E}[\sigma_c|\mathcal{H}_0] = \sigma_{bg} \tag{3.12}$$

$$\mathrm{E}[\sigma_n|\mathcal{H}_1] = \mathrm{E}[\sigma_n|\mathcal{H}_0] = P_{fg}\sigma_{fg} + P_{bg}\sigma_{bg}, \quad n \neq c \tag{3.13}$$

$$\mathrm{Var}(\sigma_n|\mathcal{H}_1) = \mathrm{Var}(\sigma_n|\mathcal{H}_0) = v, \quad \forall n \tag{3.14}$$

The pdfs of ϕ_i under $\mathcal{H}_0$ and $\mathcal{H}_1$ can now be given as

$$p(\phi_i|\mathcal{H}_1) = \frac{1}{\sqrt{2\pi v_\phi}} \exp\left(-\frac{1}{2v_\phi}(\phi_i - \mu_{\phi,1})^2\right) \tag{3.15}$$

$$p(\phi_i|\mathcal{H}_0) = \frac{1}{\sqrt{2\pi v_\phi}} \exp\left(-\frac{1}{2v_\phi}(\phi_i - \mu_{\phi,0})^2\right) \tag{3.16}$$

with which a generalised likelihood ratio test (GLRT) can be defined as

$$L_G(\phi_i) = \frac{p(\phi_i; \mathcal{H}_1)}{p(\phi_i; \mathcal{H}_0)} > \gamma \tag{3.17}$$

where γ is a threshold chosen based on the type II or false alarm probability.

If for a certain value for ϕ_m the expression in (3.17) is true, then hypothesis 1 is chosen. Otherwise, the zero hypothesis is chosen. The test giving a minimum probability of error (MPE) results from setting $\gamma = 1$ and, with the use of Bayesian theory, the test can be rewritten as

$$L_G(\phi_i) = \frac{p(\phi_i; \mathcal{H}_1)}{p(\phi_i; \mathcal{H}_1)} = \frac{p(\phi_i|\mathcal{H}_1)P(\mathcal{H}_1)}{p(\phi_i|\mathcal{H}_0)P(\mathcal{H}_0)} > 1 \tag{3.18}$$

$$\frac{p(\phi_i|\mathcal{H}_1)}{p(\phi_i|\mathcal{H}_0)} > \frac{P(\mathcal{H}_0)}{P(\mathcal{H}_1)} \tag{3.19}$$

By combining (3.15), (3.16), (3.17), (3.18) and (3.19), an expression for the detector can be derived as

$$\frac{p(\phi_i|\mathcal{H}_1)}{p(\phi_i|\mathcal{H}_0)} > \frac{P(\mathcal{H}_0)}{P(\mathcal{H}_1)} \tag{3.20}$$

$$\frac{\frac{1}{\sqrt{2\pi v_\phi}}\exp\left(-\frac{1}{2v_\phi}(\phi_i-\mu_{\phi,1})^2\right)}{\frac{1}{\sqrt{2\pi v_\phi}}\exp\left(-\frac{1}{2v_\phi}(\phi_i-\mu_{\phi,0})^2\right)} > \frac{P_{bg}}{P_{fg}} \tag{3.21}$$

$$\frac{\exp\left(-\frac{1}{2v_\phi}(\phi_i-\mu_{\phi,1})^2\right)}{\exp\left(-\frac{1}{2v_\phi}(\phi_i-\mu_{\phi,0})^2\right)} > \frac{P_{bg}}{P_{fg}} \tag{3.22}$$

$$\exp\left(\frac{1}{2v_\phi}((\phi_i-\mu_{\phi,0})^2-(\phi_i-\mu_{\phi,1})^2)\right) > \frac{P_{bg}}{P_{fg}} \tag{3.23}$$

$$\frac{1}{2v_\phi}((\phi_i-\mu_{\phi,0})^2-(\phi_i-\mu_{\phi,1})^2) > \ln P_{bg} - \ln P_{fg} \tag{3.24}$$

$$(\phi_i-\mu_{\phi,0})^2-(\phi_i-\mu_{\phi,1})^2 > 2v_\phi(\ln P_{bg} - \ln P_{fg}) \tag{3.25}$$

$$2\phi_i(\mu_{\phi,1}-\mu_{\phi,0}) + \mu_{\phi,0}^2 - \mu_{\phi,1}^2 > 2v_\phi(\ln P_{bg} - \ln P_{fg}) \tag{3.26}$$

$$\phi_i < \frac{v_\phi(\ln P_{bg} - \ln P_{fg})}{(\mu_{\phi,1}-\mu_{\phi,0})} + \frac{\mu_{\phi,1}^2-\mu_{\phi,0}^2}{2(\mu_{\phi,1}-\mu_{\phi,0})}, \quad \sigma_{fg} < \sigma_{bg} \tag{3.27}$$

If we then substitute (3.8), (3.9) and (3.10) into the expression above, then we arrive at the final expression for the block detector given by

$$\begin{aligned}\phi_i < \frac{v(\ln P_{bg} - \ln P_{fg})\sum_{n=1}^{N}\sum_{p=1}^{N}[M_\tau]_{i,n}[M_\tau]_{i,p}\rho_{n,p}}{[M_\tau]_{i,c}(\sigma_{fg}-\sigma_{bg})} + \frac{[M_\tau]_{i,c}(\sigma_{fg}^2-\sigma_{bg}^2)}{2(\sigma_{fg}-\sigma_{bg})} \\ + (P_{fg}\sigma_{fg}+P_{bg}\sigma_{bg})\sum_{n=1,n\neq c}^{N}[M_\tau]_{i,n}, \quad \sigma_{fg}<\sigma_{bg}\end{aligned} \tag{3.28}$$

From this expression, several observations can be made on the performance of the detector. First of all, the performance of the detector depends a great deal on the prior assumptions that have to be made, e.g., the prior chance of a cell belonging to a block or not, the distributions of the conductivity for both blocks and normal tissue, and the correlation between the conductivities of cells are all assumed to be known. Any differences with reality can obviously lead to a sub-optimal performance.

Secondly, it is also assumed that the sensor-to-cell distance is known, as well as the transmembrane voltages of each cell over time.

By deriving the expression in (3.28), a clear relationship is derived between how easy blocks are detected and the values of the parameters. For example, as a cell c is taken further away from the sensor, prior knowledge dominates the detection process. Decreasing the sensor-to-cell distance and/or testing closer to the AT of the cell, which means increasing the corresponding entry of M_τ since

$$[M_\tau]_{i,n} \propto \frac{1}{r_{m,n}} \tag{3.29}$$

where $r_{m,n}$ is the euclidean distance between sensor m and cell n, and sensor m is the sensor corresponding to measurement i. This makes it easier to detect blocks, because the prior information needs to be less relied upon, thus resulting in more reliable decisions. An increased or decreased conductivity variance and/or correlation between conductivity values of any to cells can either lead to easier or more difficult detection, depending on the assumed prior distribution of blocks and normal tissue.

As mentioned before, prior knowledge plays an important role in the detection process, even more so as the height increases. For example, expecting a larger part of the tissue to consist of blocks can lead to a harder detection of those blocks and vice versa.

In the light of the development of aforementioned conductivity estimation methods, the question arises whether any other inferred information, such as the conductivity estimates, can be used to adjust

the detector for specific cases. This can be done by assuming the received EGM measurement ϕ_i is constructed in the same way as how it is modelled. Then, if we use the estimated conductivities instead of the EGM measurements by substituting the left hand side of (3.28) with

$$\phi_i = \sum_{n=1}^{N} [M_\tau]_{i,n} \hat{\sigma}_n, \tag{3.30}$$

the detector can be rewritten as

$$\begin{aligned} \hat{\sigma_c} < & \frac{v(\ln P_{bg} - \ln P_{fg}) \sum_{n=1}^{N} \sum_{p=1}^{N} [M_\tau]_{i,n} [M_\tau]_{i,p} \rho_{n,p}}{[M_\tau]_{i,c}^2 (\sigma_{fg} - \sigma_{bg})} + \frac{\sigma_{fg}^2 - \sigma_{bg}^2}{2(\sigma_{fg} - \sigma_{bg})} \\ & + \sum_{n=1, n \neq c}^{N} \frac{[M_\tau]_{i,n}}{[M_\tau]_{i,c}} (P_{fg}\sigma_{fg} + P_{bg}\sigma_{bg} - \hat{\sigma}_n), \quad \sigma_{fg} < \sigma_{bg} \end{aligned} \tag{3.31}$$

Note that the accuracy of the used conductivity estimation techniques is relied upon and that obtained estimates will adjust the detector for better or worse depending on whether they are more and less accurate representations of the real conductivities. Also, since we substitute the left hand side of (3.28) by (3.30), the cell conductivity estimates are tested rather than the EGM measurements themselves, therefore not requiring the cell conductivity estimates to be true to the EGM measurements given the matrix M_τ.

3.2.2. Performance of the block detector

In the previous section, a detector was derived to decide between two proposed hypotheses, whether a certain cell of interest is part of a conduction block or not using any EGM measurement, given the cell of interest lies within range of the sensor from which the measurement is taken. The next step is to study the performance of this detector in (3.28), in particular comparing its performance in different situations i.e. for different values of the height, which is the parameter of interest. A straightforward way of doing so is to plot its region of convergence (ROC) curve, which compares its probability of detection P_D with its false alarm or type I error probability P_{FA}. The ROC curves for different values of the height of the cell of interest located directly underneath one of the sensors, were constructed in this way for a certain set of prior assumptions and values for the other involved parameters as shown in Fig. 3.2.

From the figure, it can be seen that, as the height decreases, the curve bends more and more to the upper-left of the graph. This represents the decrease of the MPE, which in turn suggests that decisions made using the detector become more accurate. Intuitively, this can also be seen as the spatial low-pass filter in the EGM model making it harder to distinguish conduction blocks from background as the height increases.

3.3. Effect on conductivity estimation for varying block size and block strength

Experimentally, the ability to detect conductivity blocks in different environments as described by the conduction block detector can be tested by studying the performance of any conductivity estimation algorithm of choice. Using such a method to estimate a conductivity map given a set of measurements from 2D simulated cardiac tissue, it is possible to study the effect of the height on its ability to estimate a conduction block of certain size and strength. In the first experiment, EGMs were simulated using the Courtemanche model for an atrial cell [17], from which a single conductivity map was estimated using the SCFA method [26] at different constant heights, which were assumed to be known. The results of this are shown in Fig. 3.3.

In this figure, the low-pass filtering effect of the height on the perceived conductivities is clearly seen. In the second experiment, blocks of different size were estimated at the same height. The results of this are shown in Fig. 3.4. Lastly, the conductivity maps were estimated for blocks of constant size and varying strength at a certain height. These results are shown in Fig. 3.5.

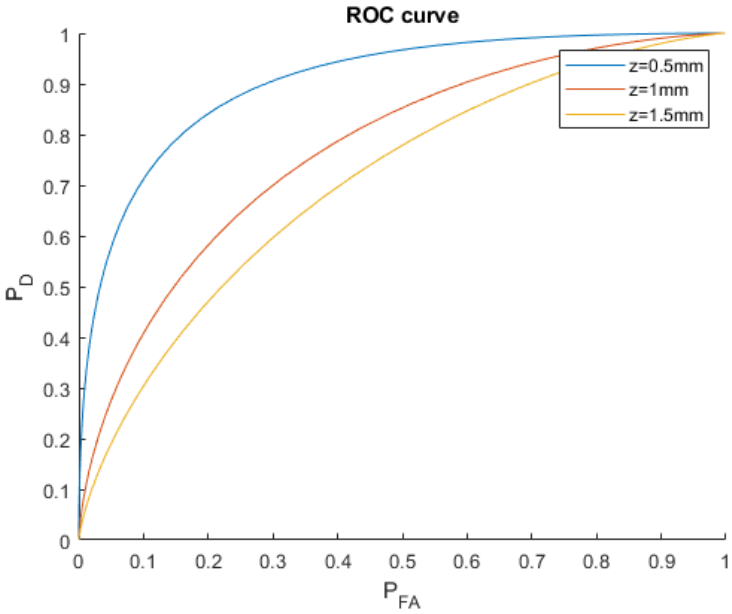

Figure 3.2: ROC curves of the block detector in (3.28) for different values of the height.

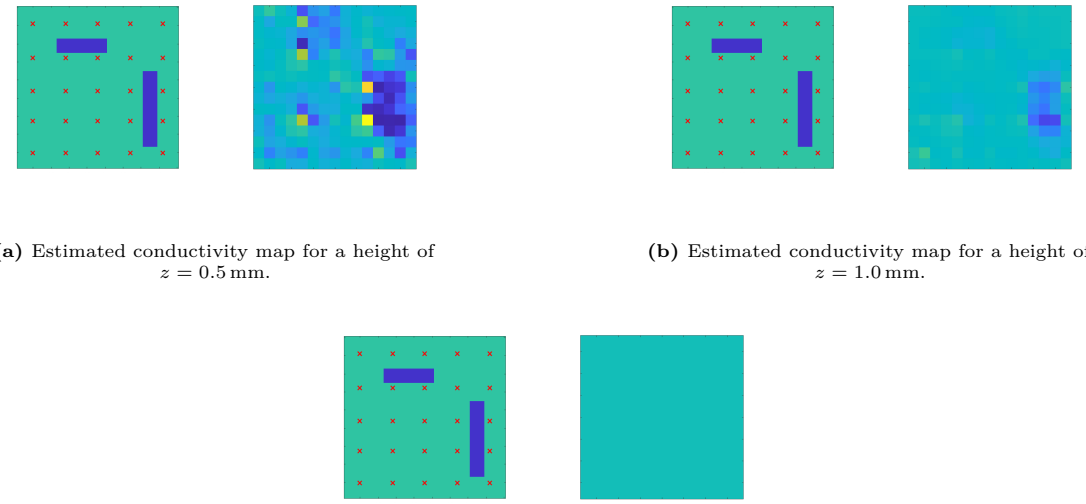

(a) Estimated conductivity map for a height of $z = 0.5\,\mathrm{mm}$.

(b) Estimated conductivity map for a height of $z = 1.0\,\mathrm{mm}$.

(c) Estimated conductivity map for a height of $z = 2.0\,\mathrm{mm}$.

Figure 3.3: Estimated conductivity maps for conductivity blocks of fixed size and strength for various values of the height on a cell grid of 45×45 cells. The normal tissue conductivity and block conductivity were set at $z = 1.0\,\mathrm{mm}$, $\sigma_{bg} = 1.1\,\mathrm{nS\,\mu m^{-1}\,pF^{-1}}$ and $\sigma_{fg} = 0.1\,\mathrm{nS\,\mu m^{-1}\,pF^{-1}}$ respectively. The red crossmarks denote the locations of the sensors.

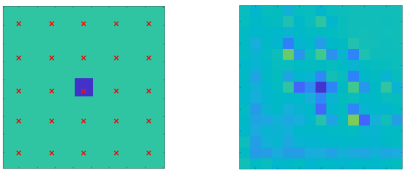

(a) Estimated conductivity map for a block with a size of 5×5 cells.

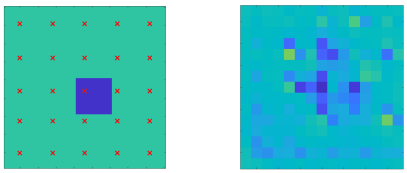

(b) Estimated conductivity map for a block with a size of 10×10 cells.

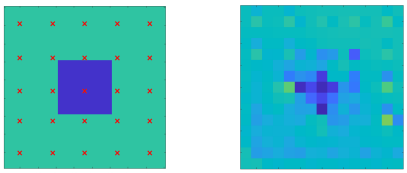

(c) Estimated conductivity map for a block with a size of 15×15 cells.

Figure 3.4: Estimated conductivity maps for conductivity blocks of varying size on a cell grid of 45×45 cells. The height, normal tissue conductivity and block conductivity were set at $z = 0.25\,\mathrm{mm}$, $\sigma_{bg} = 1.1\,\mathrm{nS\,\mu m^{-1}\,pF^{-1}}$ and $\sigma_{fg} = 0.1\,\mathrm{nS\,\mu m^{-1}\,pF^{-1}}$ respectively. The red crossmarks denote the locations of the sensors.

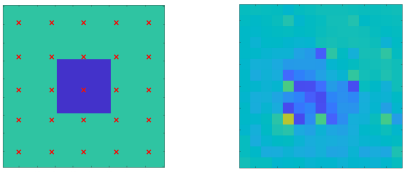

(a) Estimated conductivity map for a block with a strength of $\sigma_{bg} = 0.1\,\mathrm{nS\,\mu m^{-1}\,pF^{-1}}$.

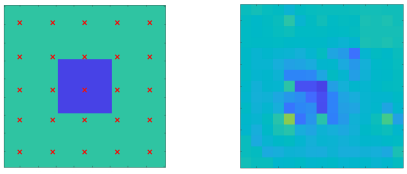

(b) Estimated conductivity map for a block with a strength of $\sigma_{bg} = 0.2\,\mathrm{nS\,\mu m^{-1}\,pF^{-1}}$.

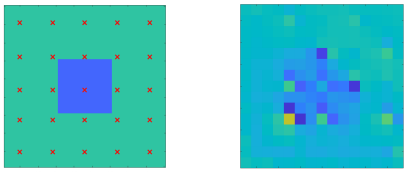

(c) Estimated conductivity map for a block with a strength of $\sigma_{bg} = 0.4\,\mathrm{nS\,\mu m^{-1}\,pF^{-1}}$.

Figure 3.5: Estimated conductivity maps for conductivity blocks of varying strength on a cell grid of 45×45 cells. The height, normal tissue conductivity and block size were set at $z = 0.25\,\mathrm{mm}$, $\sigma_{bg} = 1.1\,\mathrm{nS\,\mu m^{-1}\,pF^{-1}}$ and 15×15 cells respectively. The red crossmarks denote the locations of the sensors.

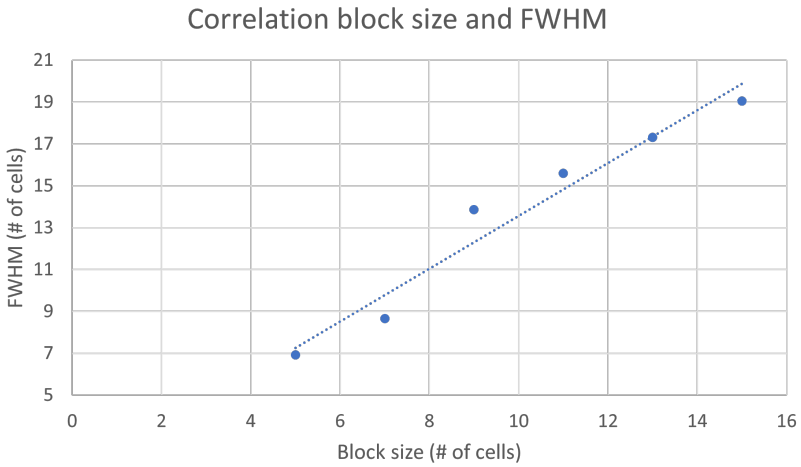

Figure 3.6: Maximum visible height versus block size, with $\sigma_{bg} = 1.1\,\mathrm{nS\,\mu m^{-1}\,pF^{-1}}$ and $\sigma_{fg} = 0.1\,\mathrm{nS\,\mu m^{-1}\,pF^{-1}}$.

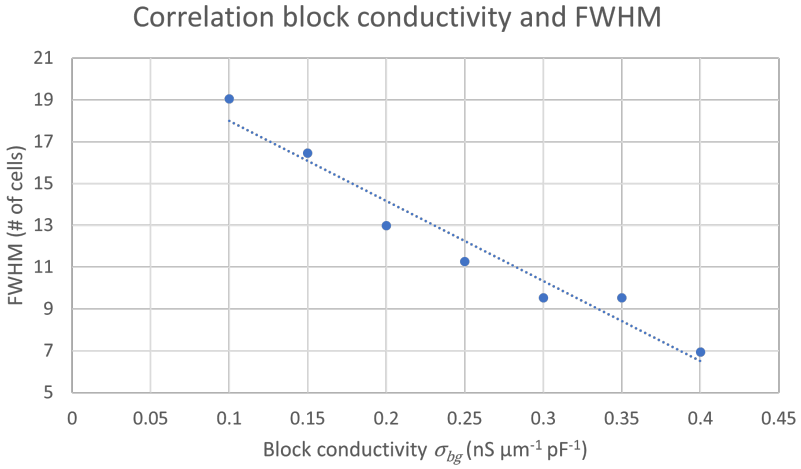

Figure 3.7: Maximum visible height versus the block conductivity σ_{fg}, with $\sigma_{bg} = 1.1\,\mathrm{nS\,\mu m^{-1}\,pF^{-1}}$ and $W_{block} \times H_{block} = 15 \times 15$ cells.

From the figures, it can indeed be seen that for smaller blocks, conductivities are spread out and the blocks lose contrast with the background. This is explained by the effect of the low-pass filter in the EGM model. Also, as blocks become less strong and cells belonging to a block take on values closer to normal tissue, detection and localisation of blocks becomes harder. By repeating the procedure and noting down at which height the blocks disappear from the map altogether, a graph can be constructed showing the relation between the block size and maximum visible height. As a measure of the height, the full width at half maximum (FWHM) is used, which is measured in numbers of modelled cells and defined as

$$\mathrm{FWHM} = \frac{2\sqrt{3}z}{d} \tag{3.32}$$

where z is the height and $d = 0.04\,\mathrm{cm}$ is the simulated width and height of a cell. These results are shown in Fig. 3.6. The same can also be done for blocks with the same size, but varying conductivities. The results of this are shown in Fig. 3.7.

The results show that there is an approximately linear correlation between the maximum visible height of a block and both its size and block strength. Just like the decrease of block visibility for smaller block sizes is explained by the low-pass spatial filter effect of the sensor-to-cell distance, the

decrease of visibility in terms of the block conductivity values can be explained with the block detector model in (3.28). Looking closely, it can be seen that as the contrast between the background and the blocks decreases, the prior information takes on a larger role in the decision-making and the actual conductivity values matter less, meaning that for optimal performance, the measured data is relied upon less. These insights can be taken into account when studying and drawing conclusions from conductivity maps estimated by the SCFA and other similar conductivity estimation methods, specifically within the context of medical diagnostics.

4

The effects of sensor-to-cell height estimation errors on the electrogram, block detection and conductivity estimation

In the previous chapter, the effect of the height on block detection and conductivity estimation was explored. At the time, the height was still considered to be known. In this chapter, the case will be considered where the height is unknown and is estimated in some way, where the focus will be on the consequences of making errors on the estimation of the height with respect to block detection and conductivity estimation.

It is important to understand what the wrong approximations of certain parameters does. This is because it makes it easier to recognise faulty behaviour of an algorithm used to estimate the parameters of interest. To fully try to grasp the impact of errors in the height estimation, we will approach the problem in two different ways using the electrogram model and the derived block detector. We will assume that the cells are located on the xy-plane, with the sensors located a certain distance away from the tissue. However in this case, the sensors do not have to be assumed to lie on a plane parallel to the tissue themselves, as will be explained.

4.1. Effect on the electrogram model

First, we recall the expressions for the discrete EGM model and the sensor-to-cell distance from Chapter 3. If we now assume a constant height of the cells with respect to a certain sensor positioned at the origin, the transfer function $h_i(\mathbf{r})$ describing the low-pass filter effect for a certain value of the sensor-to-cell height z_i from any location to that sensor can be written as

$$h_i(\mathbf{r}) = \frac{1}{\sqrt{||\mathbf{r}||_2^2 + z_i^2}} \tag{4.1}$$

where $\mathbf{r} \in \mathbb{R}^2$ is the two-dimensional location vector of the modelled cells in the xy-plane. It is obvious that for two different values for z_i, the transfer function takes a different shape. This happens for example in the case of an height estimation mismatch. A wrong estimate of the height can be interpreted as assuming a different transfer function than the true one. If we now consider the case where EGM measurements are taken of a single 2D layer of tissue at a height z_0 and an estimate of that height z_1 is made. The true transfer function and the estimated transfer function can then be compared to each other. For the case of $z_1 > z_0$ and $z_1 < z_0$, the results for are shown in Fig. 4.1 and Fig. 4.2 respectively, as a function of the magnitude $x = ||\mathbf{r}||_2$ on the horizontal axis.

What can be seen from the figures is the following. If we take the case where $z_1 > z_0$, it can be seen that the transfer function is estimated to be smaller than it should be in the vicinity of the sensor. This means that higher signal values will be mapped near the sensor, which implies a higher conductivity. This can also be seen as conductivities being overestimated in the vicinity of the sensor, which means

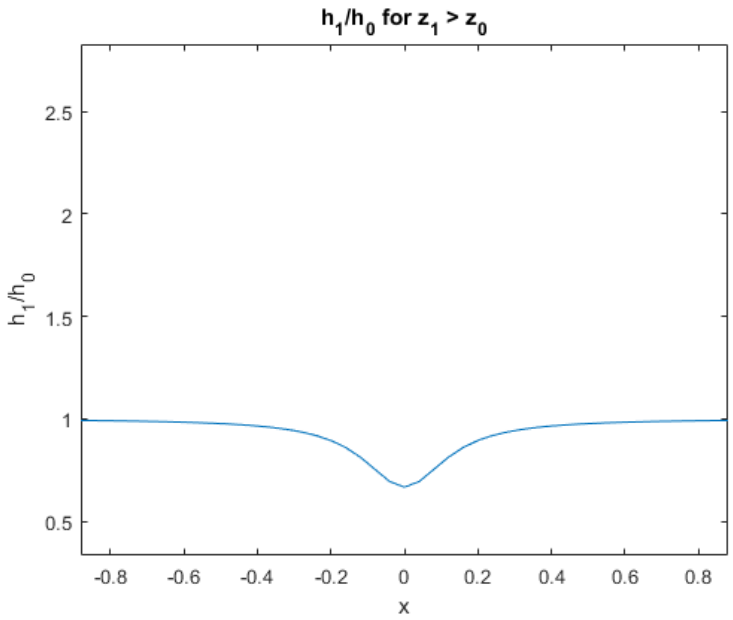

Figure 4.1: Ratio of the estimated and the true transfer function h_1/h_0 for $z_1 > z_0$.

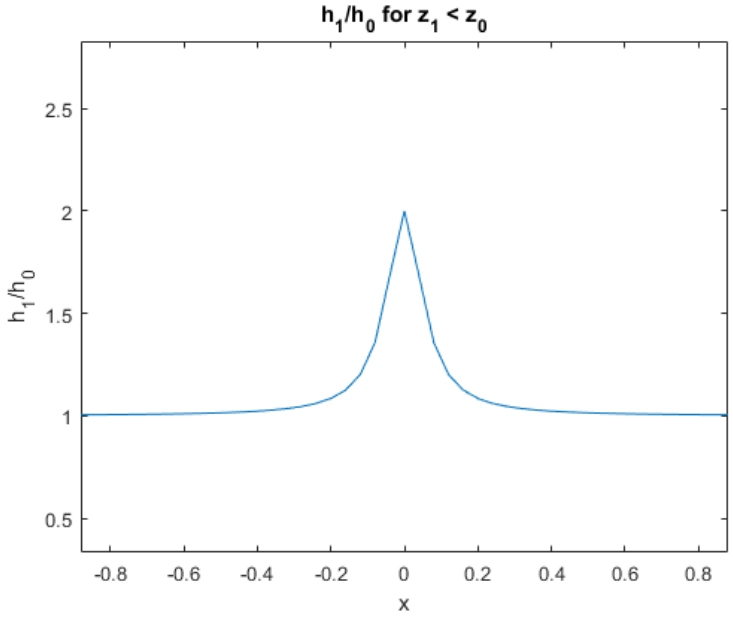

Figure 4.2: Ratio of the estimated and the true transfer function h_1/h_0 for $z_1 < z_0$.

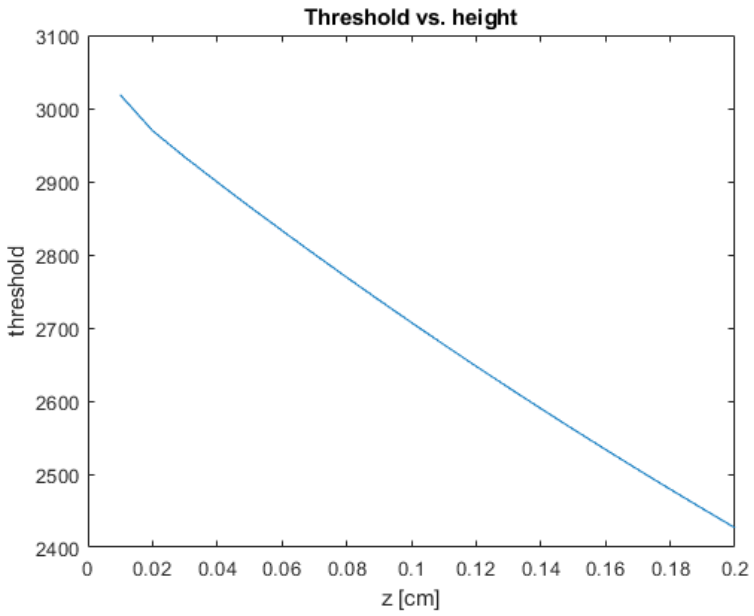

Figure 4.3: The threshold on the right-hand side of (3.28), plotted as a function of the height, z.

blocks are mapped further away from the sensor and become harder to detect. The opposite is also true. In the case where $z_1 < z_0$, the higher signal values are mapped further away, implying lower conductivities near the sensor. This can be seen as blocks being drawn towards the sensor.

4.2. Effect on the performance of the block detector

The aforementioned effect of low and high conductivities being drawn to and pushed away from the sensor locations can also be explained by taking a look at the block detector model from the previous chapter. In particular, the threshold against which the EGM measurements are compared can be plotted as a function of the height, which is done in Fig. 4.3.

In the figure it can be seen that for a certain height z_0 the threshold will take on a specific value and that the threshold decreases as the height increases. A wrong estimate z_1 of the height can then alter the threshold, which results in a sub-optimal performance of the detector. Specifically, a too low height estimate will increase the threshold, making it easier to detect blocks. The opposite case is also true for too high estimates. This can be seen as following the ROC-curve of the block detector to the left and right for the former and latter case, respectively. If we then look back at Fig. 4.4, it can indeed be seen that in general, a higher amount of normal tissue has a higher probability to be detected as blocks for a too low height estimate, and that again the opposite holds for too high estimates of the height.

4.3. Effect on conductivity estimation

The effects described by the changing transfer function and the performance of the block detector can be shown experimentally as well. An example is given in Fig. 4.4.

In the figure can also be seen what is explained before. If the height is estimated too low, low conductivity values are drawn to the sensor, creating fake conduction blocks near the sensor locations. In the opposite case, which is when it is estimated too high, high conductivity values are drawn to the sensor, resulting in the suppression of blocks in the vicinity of sensor locations.

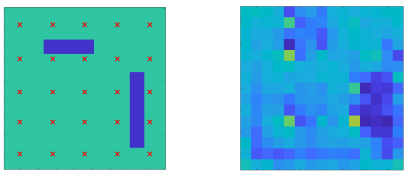

(a) Estimated conductivity map for $z_1 = 0.5\,\text{mm}$

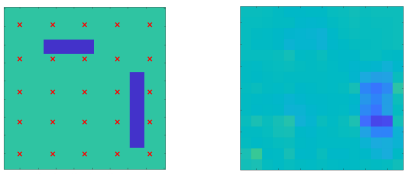

(b) Estimated conductivity map for $z_1 = 1.0\,\text{mm}$

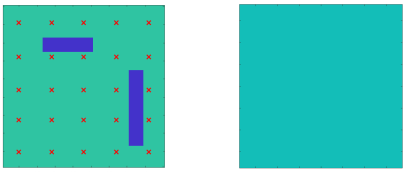

(c) Estimated conductivity map for $z_1 = 2.0\,\text{mm}$

Figure 4.4: Estimated conductivity map for different estimates z_1 of the true height $z_0 = 1.0\,\text{mm}$. The locations of the sensors are denoted by red crossmarks.

5

Sensor-to-cell height estimation

In the previous chapters, we looked at the effect of the sensor-to-cell height on the measured EGMs, the model and conductivity estimation. To this end, a block detector was derived to show the effect of the involved parameters on the ability to accurately detect blocks, as well as experiments were performed to show the behaviour predicted by the detector. Also, the effect of making estimation errors in the height was shown using the block detector and experimental data as well.

In the following chapter, the focus will lie on trying to estimate the height in cases where it is unknown and discussing how to deal with the various problems that might arise while doing so. First, the height optimisation problem is formalised and derived as its implementable form. Then, the height is estimated in different situations to study its behaviour and performance under different conditions, such as different averages and variations. Finally, since a simplified electrode model is used to model cell-specific activities other than the height, the height estimation is combined with existing conductivity estimation methods to jointly estimate the conductivity and height.

5.1. Problem analysis

First, we revisit the 2D EGM model in (2.11). By including the height as a free parameter for both the cells and the sensors, the number of dimensions of the problem changes from 2D to 3D. The 3D spatially discrete EGM model is then written as

$$\phi_m(x_m, y_m, z_m, t) = \frac{aS_v^{-1}}{4\pi\sigma_e} \sum_{n=1}^{N} \frac{\nabla \cdot \sigma(x_n, y_n, z_n) \nabla V(x_n, y_n, z_n, t)}{r_{m,n}} \tag{5.1}$$

where

$$r_{m,n} = \sqrt{(x_m - x_n)^2 + (y_m - y_n)^2 + (z_m - z_n)^2} \tag{5.2}$$

In the scope of the project we are only interested in estimating the height and not so much in any other parameters. However, assuming all parameters aside the sensor and cell locations to be known removes the necessity for any optimisation, since the EGM measurements are a linear combination of the inverse distances. This means that if the matrix holding the diffusive currents is known and invertible, the values for the height can explicitly be solved as long as the amount of measurements is equal or greater than the amount of cells. To implement some unknowns in the equation, the model in (5.1) is simplified into the form

$$\phi(x_m, y_m, z_m, t) = \frac{aS_v^{-1}}{4\pi\sigma_e} \sum_{n=1}^{N} \frac{c_n I_n(t)}{r_{m,n}} \tag{5.3}$$

where $I_n(t) = I(x_n, y_n, z_n, t)$ stands for the diffusive current of a cell n and the current weights c_n mimic the cell-specific time-independent effects of the cell on the model. Intuitively, this can be seen as

assuming the conductivity has no effect on the shape of the diffusive current apart from its amplitude. The problem can then initially be formalised as

$$\begin{aligned} &\min_{z_n, c_n} ||\boldsymbol{\phi} - \hat{\boldsymbol{\phi}}||_2^2 \\ \phi_m(t) = \phi(x_m, y_m, z_m, t) &= \frac{a}{4\pi\sigma_e} \sum_{n=1}^{N} \frac{c_n I_n(t)}{\sqrt{(x_m - x_n)^2 + (y_m - y_n)^2 + z_m^2}} \\ I_n(t) &= I_0(t - \tau_n) \\ \tau_n &= \tau(x_n, y_n) \end{aligned} \tag{5.4}$$

A quick observation can be made in the EGM model. It can be observed that changes in the height z_n of a cell can also be modelled as changes of equal effect in the weights c_n. This ambiguity is also present in the original EGM model. To bypass this ambiguity somewhat, it will be assumed that all cells are located on the xy-plane i.e. it is assumed that $z_n = 0, \forall n$. Consequently, only the sensor heights z_m need to be estimated still. This can intuitively be understood as assuming a single layer 2D tissue model where the sensors are now not located on a plane but on a separate surface away from the tissue. From another perspective, this assumption can also imply that the height does not vary in the vicinity of a sensor. The problem in (5.4) can then be rewritten as

$$\begin{aligned} &\min_{z_m, c_n} ||\boldsymbol{\phi} - \hat{\boldsymbol{\phi}}||_2^2 \\ \phi_m(t) = \phi(x_m, y_m, z_m, t) &= \frac{a}{4\pi\sigma_e} \sum_{n=1}^{N} \frac{c_n I_n(t)}{\sqrt{(x_m - x_n)^2 + (y_m - y_n)^2 + z_m^2}} \\ I_n(t) &= I_0(t - \tau_n) \\ \tau_n &= \tau(x_n, y_n) \end{aligned} \tag{5.5}$$

To make sure that the adoption of the simplified EGM model does not affect the height estimation and produces any artefacts which would not be present when we use the original model, all simulated data is made to abide by the simplified model. This is clearly a step back from reality, since in reality the derivatives of the conductivity certainly do have an effect on the received measurements. However, as stated before, the emphasis of this project lies on height estimation. The idea is to develop the right approach for height estimation, so that this can be incorporated into existing conductivity estimation methods, which are able to deal with the differential operators in the original EGM model.

However, the program as described in (5.5) does not fully solve the height estimation problem. This is because the ambiguity between the cell-specific effects and the height can not be fully solved by estimating the height per sensor instead of per cell, specifically in the case when a block is spread out over the majority of cells beneath a sensor and cells underneath other sensors. An example of this ambiguity is shown in Fig. 5.1. The cell-specific current weights c_n were put at 1.1 with 'blocks' of value 0.1 placed on the map. The height was simulated as sinusoidal function in space with an amplitude of 0.1 mm and an average value of 1.0 mm. As can be seen, a higher amount of sensors is used to show the effects of the height estimation more clearly with a higher resolution, which will be done for the remainder of this section.

As can be seen in the figure, the blocks are partially estimated, but a lot of their weights are carried over to the height estimates, resulting in huge outliers. This shows the aforementioned ambiguity. In the regions where there are no blocks, the program seems to solve the height very well. This brings us to the next step.

The goal now is to find a way to suppress the ambiguity, while keeping the rest of the estimates unaffected as much as possible. To do so, a way must be found to differentiate between the areas with blocks from those without. For this, we take a look at the activation times of the cells. For the remainder of the report, these are assumed to be known or approximated at least. For now, the true activation times will be used. What is important to keep in mind is that in real life, changes in conductivity not only have an effect on the amplitude of the recieved signals, but also on the stretching of a signal i.e. the upstroke time becomes longer when the wavefront goes from an area of high conductivity to an area of low conductivity and vice versa. This means the difference between the ATs of two adjacent

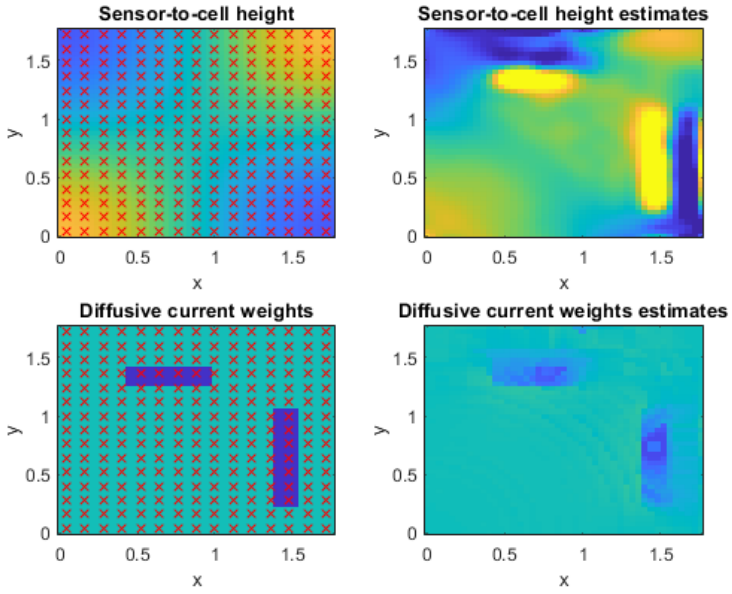

Figure 5.1: Estimated height map per cell, interpolated from the height map estimates per sensor. Blue colours denote low values and yellow colours denote high values. The red crossmarks denote the locations of the sensors.

cells becomes larger. This implies that there is information on the locations of blocks hidden in the spatial derivatives of the activation map of the simulated tissue. Therefore, we will study the ATs of the cells. The activation time of a cell n can be denoted as $\tau_n = \tau(x_n, y_n)$, where $\tau(x, y)$ is the function describing the activation map. In Fig. 5.2, the activation map can be seen, as well as the magnitude of its gradient and that of the vector with the diagonal entries of its Hessian i.e.

$$|| \operatorname{diag}(\mathbf{H}(\tau(x,y)))||_2^2 = \sqrt{\left(\frac{\partial^2 \tau(x,y)}{\partial x^2}\right)^2 + \left(\frac{\partial^2 \tau(x,y)}{\partial y^2}\right)^2} \tag{5.6}$$

where $\operatorname{diag}(A)$ is used as the vector of the diagonal entries of a matrix A, and $\mathbf{H}(f(\mathbf{x}))$ denotes the $N \times N$ Hessian matrix of a scalar function $f(\mathbf{x}), \mathbf{x} \in \mathbb{R}^N$. This expression can also be described as the magnitude of the vector holding the second derivatives of the activation map.

In Fig. 5.2 can be seen that the spatial derivatives of the activation map show high values near the edges of the blocks, specifically there where the wavefront enters it. However, the second derivatives show a similar kind of activity over a bigger area which encompasses the blocks more, whereas the first derivatives only show activity directly at the edges of the blocks. This implies that to have more information on the size of conduction blocks, information from higher derivatives should be used. In this case, the second derivatives will be used.

To summarise, the second derivatives will be used to determine the amount with which we must suppress interference from conduction blocks with the height map. The suppression is done by drawing the height to a certain average value by minimising the error between the height and that value. Combining this with the expression (5.5), the program can be rewritten as

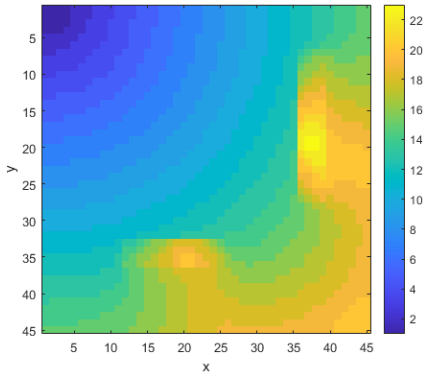

(a) The activation map for a certain set of simulated data.

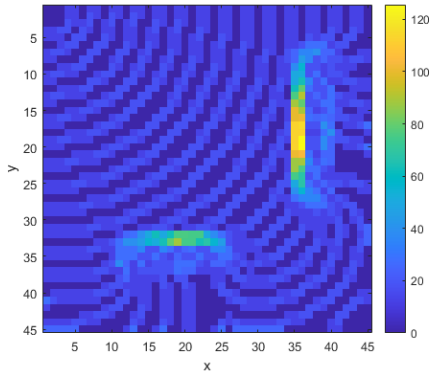

(b) The magnitude of the gradient of the activation map.

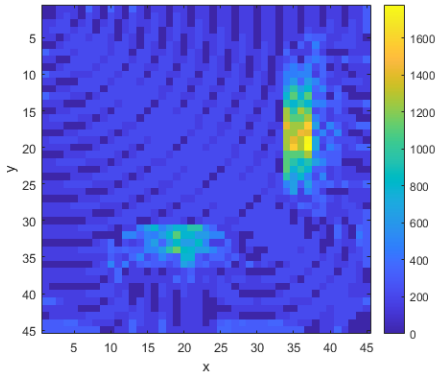

(c) The magnitude of the vector with the second order derivatives of the activation map.

Figure 5.2: Images of the activation map and the magnitude of its first and second order derivatives.

$$
\begin{aligned}
\min_{z_m, c_n} \; & ||\boldsymbol{\phi} - \hat{\boldsymbol{\phi}}||_2^2 + \lambda_1 \sum_{m=1}^{M} w_m |z_m - \mu_z| \\
w_m &= \frac{1}{|\mathcal{N}_m|} \sum_{n \in \mathcal{N}_m} w_n \\
w_n &= \text{sigm}\left(\sqrt{\left(\frac{\partial^2 \tau(x,y)}{\partial x^2} \right)^2 + \left(\frac{\partial^2 \tau(x,y)}{\partial y^2} \right)^2}, \hat{a}, \hat{b} \right) \\
\phi_m(t) = \phi(x_m, y_m, z_m, t) &= \frac{a}{4\pi\sigma_e} \sum_{n=1}^{N} \frac{c_n I_n(t)}{\sqrt{(x_m - x_n)^2 + (y_m - y_n)^2 + z_m^2}} \\
I_n(t) &= I_0(t - \tau_n) \\
\tau_n &= \tau(x_n, y_n)
\end{aligned}
\tag{5.7}
$$

where $\mathcal{N}_m$ is the set of cells underneath sensor m and $\text{sigm}(x, a, b)$ is a sigmoid activation function defined as

$$
\text{sigm}(x, a, b) = \frac{1}{1 + \exp(-a(x - b))}. \tag{5.8}
$$

The parameters a and b in the sigmoid function determine the softness of its activation and the activation threshold. For this project, these parameters were determined heuristically and denoted as $\hat{a}$ and $\hat{b}$. In (5.7) can be seen that while the activation function is determined per cell, the height is still only estimated per sensor. In practice this means that the suppression weights w_n are summed for each sensor, with the sum determining the penalty on the height for that sensor.

To further promote smoothness of the height map in order to deal with residual outliers, another term is added to the objective function. This time, as opposed to being drawn to a global average, local averages are calculated for groups of sensors, to which the height estimates are drawn. This means that the focus lies more on smoothing than constraining the height map. The calculated average is also calculated as a weighted average, with the weights w_m indicating the reliability of the height estimate under sensor m. By adding this to the expression in (5.7), the height estimation program for the simplified EGM model can be written as

$$
\begin{aligned}
\min_{z_m, c_n} \; & ||\boldsymbol{\phi} - \hat{\boldsymbol{\phi}}||_2^2 + \lambda_1 \sum_{m=1}^{M} w_m |z_m - \mu_z| + \lambda_2 \sum_{g=1}^{G} \sum_{m \in \mathcal{M}_g} (z_m - \bar{z}_g)^2 \\
w_m &= \frac{1}{|\mathcal{N}_m|} \sum_{n \in \mathcal{N}_m} w_n \\
w_n &= \text{sigm}\left(\sqrt{\left(\frac{\partial^2 \tau(x,y)}{\partial x^2} \right)^2 + \left(\frac{\partial^2 \tau(x,y)}{\partial y^2} \right)^2}, \hat{a}, \hat{b} \right) \\
\bar{z}_g &= \frac{\sum_{m \in \mathcal{M}_g} (1 - w_m) z_m}{\sum_{m \in \mathcal{M}_g} (1 - w_m)} \\
\phi_m(t) = \phi(x_m, y_m, z_m, t) &= \frac{a}{4\pi\sigma_e} \sum_{n=1}^{N} \frac{c_n I_n(t)}{\sqrt{(x_m - x_n)^2 + (y_m - y_n)^2 + z_m^2}} \\
I_n(t) &= I_0(t - \tau_n) \\
\tau_n &= \tau(x_n, y_n)
\end{aligned}
\tag{5.9}
$$

where $\mathcal{N}_m$ is the set of cells in the neighbourhood of sensor m and $\mathcal{M}_g$ is the set of sensors belonging to group g.

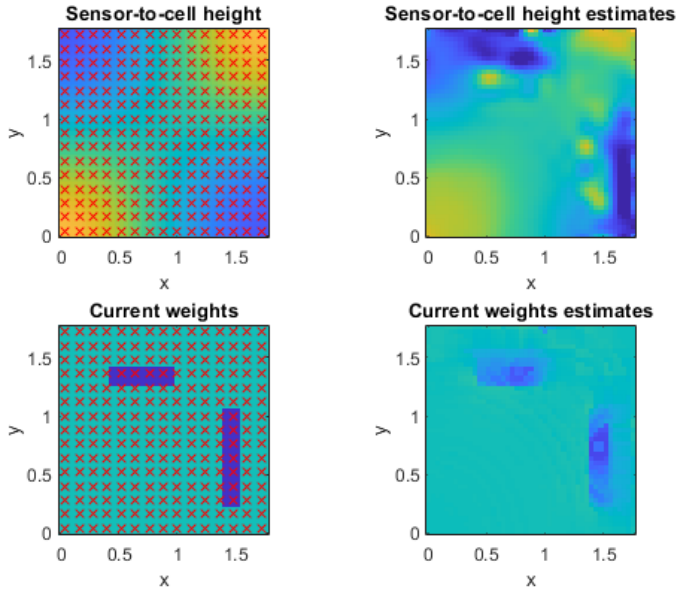

Figure 5.3: Estimated height map per cell using the simplified EGM model, for sensors groups of size 3×3, with $\lambda_1 = 1 \cdot 10^5$ and $\lambda_2 = 1 \cdot 10^6$, interpolated from the height map estimates per sensor. Blue colours denote low values and yellow colours denote high values. The red crossmarks denote the locations of the sensors.

5.2. Results

5.2.1. Height estimation

The problem in (5.9) was implemented in Matlab and solved with an interior point strategy using a native solver. The solver was set up to iterate until an optimum or a predetermined maximum amount of iterations is reached. The performance of the height estimation algorithm was checked by changing the parameters of the height map of the simulated tissue. For these tests, there were assumed a number of $M = 15 \times 15$ sensors placed in a grid of $N = 45 \times 45$ cells, an intercellular distance of $D_x = D_y = 400\,\mu\text{m}$, normal current weight $c_{bg} = 1.1$ and conductivity block current weight $c_{fg} = 0.1$ respectively. The penalisation parameters were determined heuristically and set at $\lambda_1 = 1 \cdot 10^5$ and $\lambda_2 = 1 \cdot 10^6$ respectively. The weights c_n were initialised at $c_{n,0} = 1$ and the sensor-to-cell heights were initialised at the average height value of each test. The algorithm was run for 15 iterations.

First of all, by changing the problem to its form in (5.9), the results were improved drastically. The ambiguity, as much as it was present previously, could almost be completely resolved, as is shown in Fig. 5.3.

Secondly, During follow-up tests, different parameters of the problem were varied separately to study their effects on the performance of the the height estimation, which is measured in the form of the mean square error (MSE) of the true height map with the estimated height map. These parameters included the average height, the maximum amplitude of the height, the maximum spatial frequency of the height and the size of the sensor groups. The results of the tests are shown in Fig. 5.4.

From the figures, a clear relationship can be seen between the observed parameters and the performance of the algorithm. In Fig. 5.4a can be seen that as the average height increases, it becomes harder to make good estimates of the height map and the diffusive current weights, which is to be expected. A larger height on average means in general a bigger loss of information. If we instead increase the maximum amplitude of the height as shown in Fig. 5.4b, the error gets larger as well, which could either be caused by a wrong estimate of the current weights, or because of a too low number of iterations. In 5.4c can be seen that the error increases gradually as the variations in the height increase. The graph shows some deviations from its trend, which can be explained by the coincidental overlap of current weight structures and structures created by the high variations in the height map.

Lastly, different group sizes were also tested for their effect on the height estimation. Sensor grouping was supposed to smooth the map, therefore getting rid of any outliers caused by the residual blocks. It can be seen in 5.4d that the error decreases slightly with the increase of the group size, but the yield is

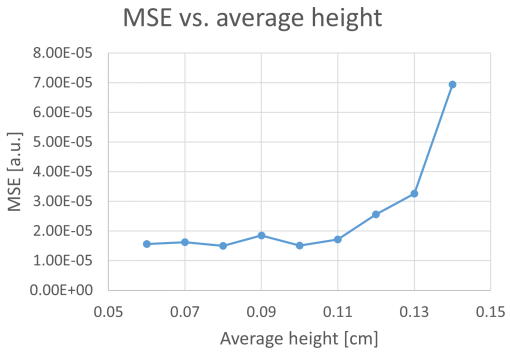

(a) The error of the estimated height map for different values of average value of the height map.

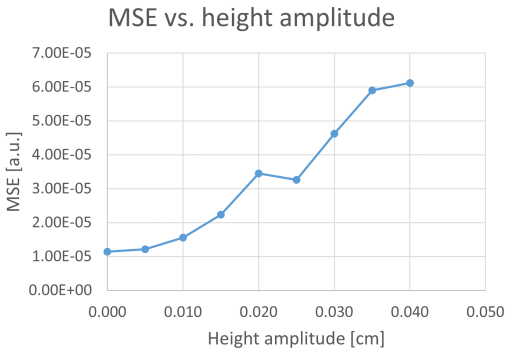

(b) The error of the estimated height map for different values of the maximum amplitude of the height map.

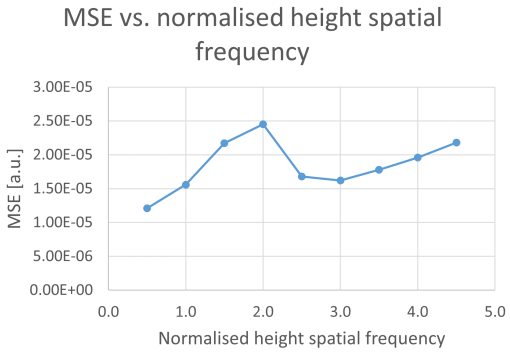

(c) The error of the estimated height map for different spatial frequencies present in the height map.

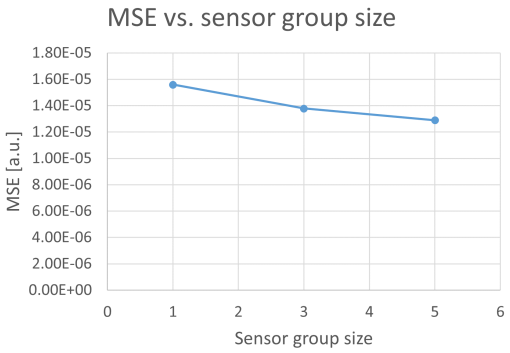

(d) The error of the estimated height map for different sensor group sizes.

Figure 5.4: The error of the estimated height map for different values of several parameters of the height map.

very small.

5.2.2. Joint conductivity and height estimation

Before, the height was estimated from data assuming a simplified model for the EGM. However, this is not consistent with reality, since the signals coming from the tissue generally have a more complex morphology. This requires that in general, the standard EGM model needs to be used as given by (5.1) and (5.2). The problem as given in (5.9) can then be written as

$$\begin{aligned}
\min_{z_m,\sigma_n} ||\boldsymbol{\phi} - \hat{\boldsymbol{\phi}}||_2^2 + \lambda_1 \sum_{m=1}^{M} w_m |z_m - \mu_z| + \lambda_2 \sum_{g=1}^{G} \sum_{m\in\mathcal{M}_g} (z_m - \bar{z}_g)^2 \\
w_m = \frac{1}{|\mathcal{N}_m|} \sum_{n\in\mathcal{N}_m} w_n \\
w_n = \text{sigm}\left(\sqrt{\left(\frac{\partial^2\tau(x,y)}{\partial x^2}\right)^2 + \left(\frac{\partial^2\tau(x,y)}{\partial y^2}\right)^2}, \hat{a}, \hat{b}\right) \\
\bar{z}_g = \frac{\sum_{m\in\mathcal{M}_g}(1-w_m)z_m}{\sum_{m\in\mathcal{M}_g}(1-w_m)} \\
\phi_m(t) = \phi(x_m, y_m, z_m, t) = \frac{a}{4\pi\sigma_e} \sum_{n=1}^{N} \frac{\nabla\cdot\sigma_n\nabla V_n(t)}{\sqrt{(x_m-x_n)^2 + (y_m-y_n)^2 + z_m^2}} \\
V_n(t) = V_0(t-\tau_n) \\
\tau_n = \tau(x_n, y_n)
\end{aligned} \tag{5.10}$$

Similarly as what was done using the simplified model, the algorithm was performed on the same data. This time, with the values for the current weight used as the cell conductivity values in the appropriate units. The penalisation parameters were increased somewhat to values of $\lambda_1 = 1 \cdot 10^9$ and $\lambda_2 = 1 \cdot 10^{10}$, due to the fact that the initial value of the first term was increased by some orders of magnitude as well. The results are shown in Fig. 5.5. Comparing it to Fig. 5.3, it is obvious that the performance is worse. Although there is little interference from conductivity blocks, the height is estimated have a much lower amplitude than is the case. Despite that, the general features of the height map can still be distinguished, albeit that they are less prominent. This can be the result of convergence to a local minimum. Further testing with adjusted tolerances and parameters and more iterations of the algorithm showed no significant improvements to the visual aspects of the height map.

5.2.3. Performance with estimated height versus assumed height

In the aforementioned method, joint conductivity and height estimation is attempted with the designed algorithm. However, as seen before, methods exist which are undoubtedly better at estimating the conductivities than the simple solution in the previous section. The question therefore arises whether, while ignoring the conductivity estimates, the height estimates would be able to increase the performance of the existing methods. To answer this question, the following procedure is applied. First, for a certain conductivity map and a constant height, the height and conductivities are estimated using the designed algorithm. Then, the initial conductivity estimates are discarded, whereas the height estimates are fed to an existing conductivity estimation algorithm, which in this case will be the SCFA algorithm. This algorithm then uses the estimated height map to estimate the conductivities. The results of this are compared to the several situations where the height map is not estimated, but randomly assumed or guessed. All the same settings are used to simulate data and estimate parameters as before.

For the first test, a true height map of $z_0 = 0.1\,\text{cm}$ is chosen. Then, the height is estimated and stored in z_{est}. To compare, the conductivities were also estimated for assumed values of the height, labelled z_{asd}, near the true value. The error ϵ_σ was than plotted against the assumed height. The same procedure was followed with $z_0(x, y) = 0.05\,\text{cm}$. The results are shown in Fig. 5.6.

What can be seen from the results is that first of all, the error in the conductivities is lowest when assuming the correct height, as is expected. Then, as the assumed height is taken further from the true height, the error increases. At some point, the error with the assumed height exceeds the error with the

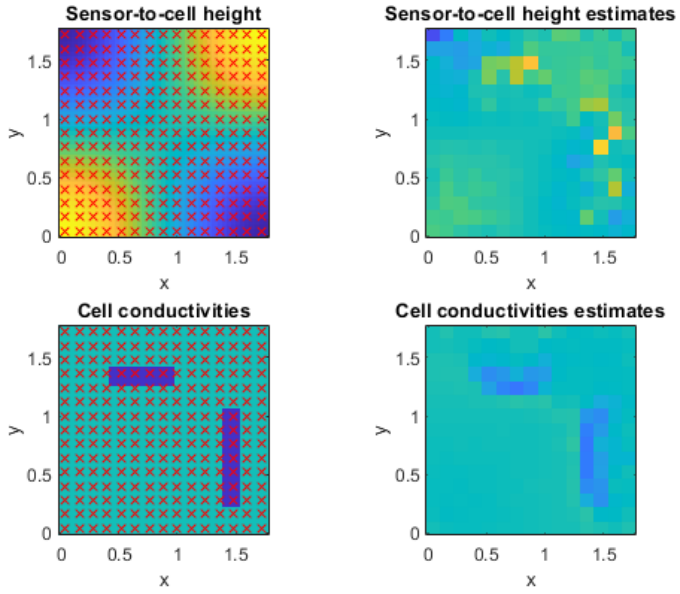

Figure 5.5: Estimated height map per cell using the standard EGM model, for sensors groups of size 3×3, with $\lambda_1 = 1 \cdot 10^9$ and $\lambda_2 = 1 \cdot 10^{10}$, interpolated from the height map estimates per sensor. Blue colours denote low values and yellow colours denote high values. The red crossmarks denote the locations of the sensors.

estimated height. This means that at that point, the performance using the estimated height from the designed algorithm is better than any guess that is made at that point. Depending on how well people are able to take a guess at the true height, our algorithm should be able to provide a good baseline in terms of maximally possible errors. If we also look more closely to Fig. 5.6b, it can be seen that the lowest error of the conductivity map did not result from the assumed height equal to the true height and even that the estimated height gives better results than the true height. This can be explained by the fact that the SCFA method solves a non-convex problem, which means that it is not guaranteed to reach a global optimum. It is safe to say that there is a high probability that in reality the performance for $z_0 = 0.05\,\text{cm}$ is more akin to the case of $z_0 = 0.1\,\text{cm}$, with the estimated height having a range of confidence of ca. $0.01 - 0.02\,\text{cm}$.

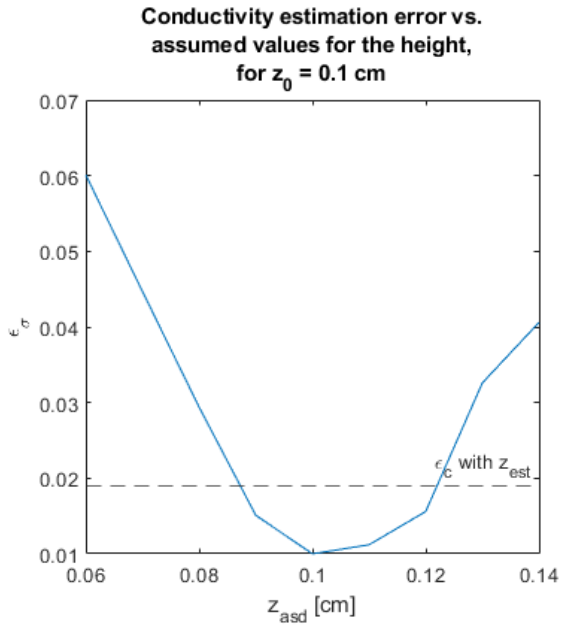

(a) Error ϵ_σ of the estimated conductivity map with the true conductivity map for $z_0 = 0.1\,\text{cm}$.

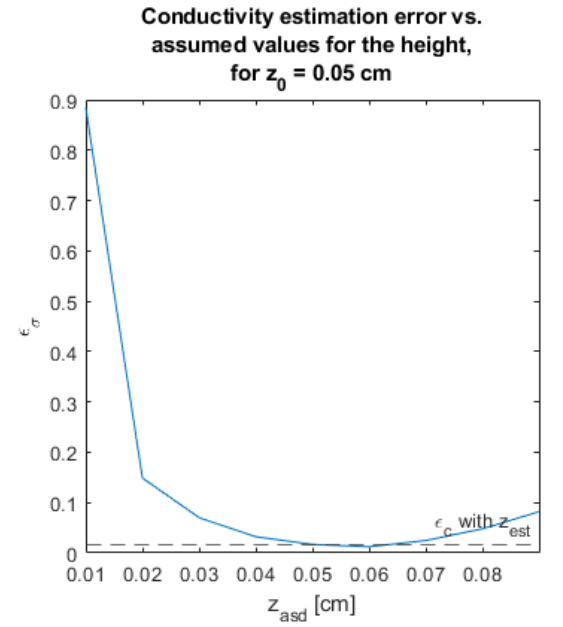

(b) Error ϵ_σ of the estimated conductivity map with the true conductivity map for $z_0 = 0.05\,\text{cm}$.

Figure 5.6: Error ϵ_σ of the estimated conductivity map with the true conductivity map using the SCFA algorithm using assumed values for the height z_{asd} near different values of the true height z_0. As a comparison, the error using the estimated height z_{est} from the designed algorithm is shown with the dashed lines.

6

Conclusion

The goal of the project was to investigate the height between the sensors of the sensor array used for atrial mapping and the cardiac cells, which is one of the many parameters involved in recording and extracting information from EGMs, and its role in the inference of information about the cardiac tissue. Specifically, the effect of the height on the measured data, the effect of estimation errors of the height on the inference of information from the measured data and the ways of estimating the height from the measured data were investigated.

Several steps were taken in order to understand how the height influences the measured data. First, the height parameter was considered as a parameter in the standard model for the EGM to show its effects on the received data. This showed that the height acts as a spatial low-pass filter or blurring on the electrical signals from the heart received by the sensors. Secondly, a detector was derived for determining whether a certain cell of interest belongs to conduction block or not by assigning prior distributions of the conductivity and utilising the linear relationship between the cell conductivities and the EGM. By examining the behaviour and performance of this detector in different circumstances, the effect of the height was found, as well as that of other parameters. Thirdly, the observations done with use of both the EGM model and the block detector were then confirmed by the experimental data.

In order to understand the severity of a lack of information on the height in the context of estimation of the tissue parameters, the effect of estimation errors was shown by observing how measured data is affected differently by different heights and how this might warp our vision of the underlying tissue. Experimentally, this was shown as specific changes in the spatial distribution of the cell conductivities. In addition, this effect could be explained using the previously derived block detector.

Ultimately, the goal of the project was finding a way of estimating the height. From early observations was seen how hard it is to distinguish between the effects of the cell conductivity strengths and the sensor-to-cell height on the data due to their ambiguous interactions. To increase feasibility, a simplified EGM model was considered, which exchanged a great deal of the range of applications for a better overall performance. Starting with the minimisation of a standard objective function describing the mean-squared error between the measured and estimated EGM data, other constraints were introduced to the objective function in order to constrain the solution space of the optimisation problem. It was shown that the height could be estimated to a certain extend and how the performance is affected by the layout of the height map and choice of parameters in the optimisation problem. The fact that the simplified EGM model provides better results suggests that more similarity in morphology of the signals from each cell results in better results.

After that, a follow-up implementation was tested using the standard EGM model. From the results was seen how the algorithm was able to provide a plausible height map, albeit that convergence ceased rather quickly after running the algorithm, which could not simply be fixed by running the algorithm for a longer time. However, the general features of the true height map could still be distinguished.

Then, instead of estimating the height and conductivity simultaneously, the height was estimated on its own and subsequently fed to the SCFA algorithm in order to estimate the conductivities. The results where compared to different assumptions for the value of the height near the true height. It was then seen that our algorithm showed an increase in performance when the assumed height went beyond a certain range around the true height. This means that our algorithm increases the reliability of the

conductivity estimation depending on how prone people are to take guesses at the value for the height further away from the true height.

This project has been able to provide insight in the effect of the sensor-to-cell height on measured data and the effect of estimation errors in the height, as well as it showed ways to approach the height estimation problem. Despite the effects of the height and differences therein being reasonably clear, there is still much to be gained with regard to the height estimation. The difficulty of estimating the height is mostly because of the ambiguity between the effects of the height and the cell conductivities on the measured data. This becomes evident from the fact that the height and the cell conductivities overlap in space and the frequency domain. This makes it hard to separate their separate contributions to the measured data. Further research could therefore also include methods of separating the activity of the two.

References

[1] V. Jacquemet, A. Van Oosterom, J.-M. Vesin, and L. Kappenberger, "Analysis of electrocardiograms during atrial fibrillation," *IEEE engineering in medicine and biology magazine*, vol. 25, no. 6, pp. 79–88, 2006.

[2] B. Abdi, "Atrial fibrillation fingerprinting," Ph.D. dissertation, Delft University of Technology, 2021.

[3] P. Langley, J. J. Rieta, M. Stridh, J. Millet, L. Sornmo, and A. Murray, "Comparison of atrial signal extraction algorithms in 12-lead ecgs with atrial fibrillation," *IEEE Transactions on Biomedical Engineering*, vol. 53, no. 2, pp. 343–346, 2006.

[4] J. J. Rieta and F. Hornero, "Comparative study of methods for ventricular activity cancellation in atrial electrograms of atrial fibrillation," *Physiological measurement*, vol. 28, no. 8, p. 925, 2007.

[5] ThoughCo. "Evolution of the human heart." (), [Online]. Available: `https://www.thoughtco.com/evolution-of-the-human-heart-1224781` (visited on 02/03/2022).

[6] V. C. Healtcare. "Sinus node dysfunction." (), [Online]. Available: `https://www.valleychildrens.org/heart/conditions/sinus-node-dysfunction` (visited on 02/03/2022).

[7] T. Key. "Pathophysiology of cardiac arrhythmias: Arrhythmogenesis and types of arrhythmias." (), [Online]. Available: `https://thoracickey.com/pathophysiology-of-cardiac-arrhythmias-arrhythmogenesis-and-types-of-arrhythmias/` (visited on 02/03/2022).

[8] A. Yaksh, L. J. van der Does, C. Kik, *et al.*, "A novel intra-operative, high-resolution atrial mapping approach," *Journal of Interventional Cardiac Electrophysiology*, vol. 44, no. 3, pp. 221–225, 2015.

[9] A. Buttu, "Novel ecg and intracardiac electrograms signal processing schemes for predicting the outcome of atrial fibrillation catheter ablation," Ph.D. dissertation, Oct. 2014.

[10] J. M. de Bakker, "Electrogram recording and analyzing techniques to optimize selection of target sites for ablation of cardiac arrhythmias," *Pacing and Clinical Electrophysiology*, vol. 42, no. 12, pp. 1503–1516, 2019. DOI: `https://doi.org/10.1111/pace.13817`. eprint: `https://onlinelibrary.wiley.com/doi/pdf/10.1111/pace.13817`. [Online]. Available: `https://onlinelibrary.wiley.com/doi/abs/10.1111/pace.13817`.

[11] B. Abdi, A.-J. Van Der Veen, N. M. de Groot, and R. C. Hendriks, "Local activation time estimation in fractionated electrograms of cardiac mappings," in *2019 41st Annual International Conference of the IEEE Engineering in Medicine and Biology Society (EMBC)*, IEEE, 2019, pp. 285–288.

[12] D. Noble, A. Garny, and P. J. Noble, "How the hodgkin–huxley equations inspired the cardiac physiome project," *The Journal of physiology*, vol. 590, no. 11, pp. 2613–2628, 2012.

[13] A. L. Hodgkin and A. F. Huxley, "A quantitative description of membrane current and its application to conduction and excitation in nerve," *The Journal of physiology*, vol. 117, no. 4, p. 500, 1952.

[14] A. L. Hodgkin, "The croonian lecture-ionic movements and electrical activity in giant nerve fibres," *Proceedings of the Royal Society of London. Series B-Biological Sciences*, vol. 148, no. 930, pp. 1–37, 1958.

[15] A. L. Hodgkin and A. F. Huxley, "Propagation of electrical signals along giant nerve fibres," *Proceedings of the Royal Society of London. Series B-Biological Sciences*, vol. 140, no. 899, pp. 177–183, 1952.

[16] A. L. Hodgkin and A. F. Huxley, "The components of membrane conductance in the giant axon of loligo," *The Journal of physiology*, vol. 116, no. 4, p. 473, 1952.

[17] M. Courtemanche, R. J. Ramirez, and S. Nattel, "Ionic mechanisms underlying human atrial action potential properties: Insights from a mathematical model," *American Journal of Physiology-Heart and Circulatory Physiology*, vol. 275, no. 1, H301–H321, 1998.

[18] B. J. Roth, "Action potential propagation in a thick strand of cardiac muscle.," *Circulation research*, vol. 68, no. 1, pp. 162–173, 1991.

[19] R. C. Barr and R. Plonsey, "Propagation of excitation in idealized anisotropic two-dimensional tissue," *Biophysical journal*, vol. 45, no. 6, pp. 1191–1202, 1984.

[20] R. Clayton, O. Bernus, E. Cherry, *et al.*, "Models of cardiac tissue electrophysiology: Progress, challenges and open questions," *Progress in biophysics and molecular biology*, vol. 104, no. 1-3, pp. 22–48, 2011.

[21] N. Virag, V. Jacquemet, C. Henriquez, *et al.*, "Study of atrial arrhythmias in a computer model based on magnetic resonance images of human atria," *Chaos: An Interdisciplinary Journal of Nonlinear Science*, vol. 12, no. 3, pp. 754–763, 2002.

[22] C. S. Henriquez, "A brief history of tissue models for cardiac electrophysiology," *IEEE Transactions on Biomedical Engineering*, vol. 61, no. 5, pp. 1457–1465, 2014.

[23] D. B. Geselowitz and W. Miller, "A bidomain model for anisotropic cardiac muscle," *Annals of biomedical engineering*, vol. 11, no. 3, pp. 191–206, 1983.

[24] M. Potse, B. Dubé, J. Richer, A. Vinet, and R. M. Gulrajani, "A comparison of monodomain and bidomain reaction-diffusion models for action potential propagation in the human heart," *IEEE Transactions on Biomedical Engineering*, vol. 53, no. 12, pp. 2425–2435, 2006.

[25] B. M. Johnston and P. R. Johnston, "Approaches for determining cardiac bidomain conductivity values: Progress and challenges," *Medical & biological engineering & computing*, vol. 58, no. 12, pp. 2919–2935, 2020.

[26] M. Sun, N. M. de Groot, and R. C. Hendriks, "Cardiac tissue conductivity estimation using confirmatory factor analysis," *Computers in Biology and Medicine*, vol. 135, p. 104 604, 2021.

[27] R. Caulier-Cisterna, S. Muñoz-Romero, M. Sanroman-Junquera, A. García-Alberola, and J. L. Rojo-Álvarez, "A new approach to the intracardiac inverse problem using laplacian distance kernel," *Biomedical engineering online*, vol. 17, no. 1, pp. 1–25, 2018.

[28] B. Abdi, M. S. van Schie, N. M. de Groot, and R. C. Hendriks, "Analyzing the effect of electrode size on electrogram and activation map properties," *Computers in Biology and Medicine*, vol. 134, p. 104 467, 2021.

[29] B. Abdi, R. C. Hendriks, A.-J. van der Veen, and N. M. De Groot, "Ventricular activity signal removal in atrial electrograms of atrial fibrillation.," in *BIOSIGNALS*, 2019, pp. 179–184.

[30] M. Sun, E. Isufi, N. M. de Groot, and R. C. Hendriks, "Graph-time spectral analysis for atrial fibrillation," *Biomedical Signal Processing and Control*, vol. 59, p. 101 915, 2020.

[31] B. Abdi, R. C. Hendriks, A.-J. van der Veen, and N. M. de Groot, "A compact matrix model for atrial electrograms for tissue conductivity estimation," *Computers in biology and medicine*, vol. 107, pp. 284–291, 2019.

[32] ——, "Local activation time annotation in atrial electrogram arrays using deconvolution," in *2019 Computing in Cardiology (CinC)*, IEEE, 2019, Page–1.